

Direct measurement of the $\bar{K}N \rightarrow \pi\Sigma$ scattering amplitude below the $\bar{K}N$ threshold employing the $d(K^-, N)\pi\Sigma^-$ reaction

Kentaro Inoue

July 31, 2025

Contents

1	Introduction	4
1.1	Discovery of the $\Lambda(1405)$	4
1.2	$\bar{K}N$ interaction	5
1.3	Two pole strcture of the $\Lambda(1405)$	6
1.4	Recent experimental status of the $\Lambda(1405)$	7
1.5	Recent theoritical status of the $\Lambda(1405)$	7
1.6	$d(K^-, n)$ reaction	9
1.7	The J-PARC E31 experiment	11
2	Experimental setup	13
3	Analysis	14
4	$\pi\Sigma$ Spectra	15
4.1	Decomposition of the $K^-d \rightarrow n\pi^+\pi^-n$ events	15
4.1.1	Backward $\pi^\mp\Sigma^\pm$ event selection	15
4.1.2	Template fitting	17
4.2	Conversion to the cross section	24
4.2.1	Acceptance correction	24
4.2.2	Conversion factors for the cross section	27
5	Discussion	32
5.1	Spectra	32
5.1.1	Qualitative properties of obtained spectra	32
5.1.2	Comparison with theoritical calculations	34
5.1.3	$\bar{K}N$ Pole parameters assuming the 2-step reaction . .	40
6	Conclusion	49
A	$\pi^0\Sigma^0$ spectrum analysis	50

<i>CONTENTS</i>	3
B Detector resolution	51
B.1 CDC resolution	51
B.2 Detector resolution on the $d(K^-, N)$	52
C $d(K^-, n)K^0n$ analysis	53

Chapter 1

Introduction

1.1 Discovery of the $\Lambda(1405)$

The $\Lambda(1405)$ is a hyperon with strangeness $S = -1$, isospin $I = 0$ and spin and spin parity $J^P = (\frac{1}{2})^-$. In the Particle Data Group (PDG) [1], the mass and the width of the $\Lambda(1405)$ are assigned to $1405.1^{+1.3}_{-1.0}\text{MeV}$ and $50.5 \pm 2.0\text{MeV}$ respectively, based on several papers [2–4].

The existence of the $\Lambda(1405)$ was predicted for the first time by R. H. Dalitz and S. F. Taun in 1959 as a quasi-bound state of $\bar{K}N$ [5]. The candidate was reported in the $K^-p \rightarrow \pi\pi\pi\Sigma$ reaction at the Lawrence Radiation Laboratory in 1961 [6]. The excess was reported in the neutral $\pi\Sigma$ spectrum, $K^-p \rightarrow \pi^\pm\pi^\mp(\pi\Sigma)^0$, in the $\Lambda(1405)$ region compared to the doubly charged spectrum, $K^-p \rightarrow \pi^+\pi^+(\pi^-\Sigma^-)$ or $K^-p \rightarrow \pi^-\pi^-(\pi^+\Sigma^+)$, in this paper. However, there was not enough statistical data to discuss lineshape.

In order to solve these problems, R. J. Hemingway reported high-statistics $\pi^+\Sigma^-$ and $\pi^-\Sigma^+$ spectra using the $K^-p \rightarrow \pi^-\Sigma^+(1660) \rightarrow \pi^-\pi^+(\pi^\mp\Sigma^\pm)$ with $4.2\text{ GeV}/c$ K^- beam [7]. In these spectra, the momentum transfer was restricted to, $t(K^-, \pi^-) < 1.0\text{ GeV}/c$, in order to increase the purity of $\Sigma^+(1660)$. As a result, the $\Sigma^+ \rightarrow \pi^0 p$ decay event of the $K^-p \rightarrow \pi^-\Sigma^+(1660) \rightarrow \pi^-\pi^+(\pi^-\Sigma^+)$ reaction gave a $\pi^-\Sigma^+$ spectrum with almost no background. R. H. Dalitz and A. Deloff obtained the mass and width of the $\Lambda(1405)$ as $1406.4 \pm 4.0\text{ MeV}$ and $50 \pm 2\text{ MeV}$ [2] by adapting the M-matrix method to this spectrum, and these parameters were adopted for the PDG. On the other hand, the $\pi^+\Sigma^-$ spectrum of the $K^-p \rightarrow \pi^-\Sigma^+(1660) \rightarrow \pi^-\pi^+(\pi^+\Sigma^-)$ reaction had a background due to the ambiguity of the origin of the π^- . Thus, the mass spectrum of $\Lambda(1405)$ was investigated using the K^-p reaction with pion emission.

1.2 $\bar{K}N$ interaction

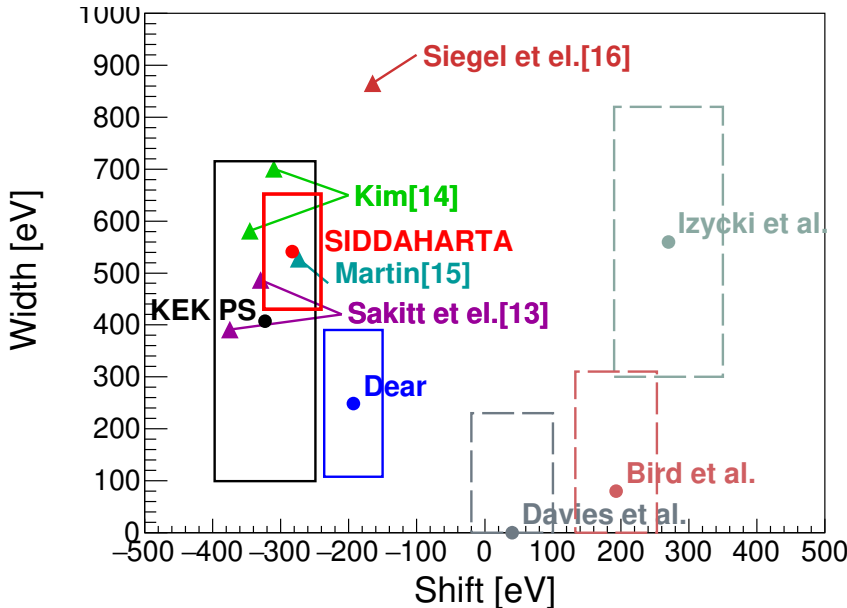


Figure 1.1: This figure is shown about the kaonic hydrogen. Triangle markers indicate theoretical calculations where $\bar{K}N$ scattering data were extrapolated to the $\bar{K}N$ threshold. Circle markers represent experimental values, and error ranges in the energy shift and width are indicated by squares. Dashed lines correspond to experiments using hydrogen gas targets conducted prior to 1990, while solid lines represent experiments conducted afterward.

Considering the $\Lambda(1405)$ as a $\bar{K}N$ bound state, the $\bar{K}N$ interaction is expected to be attractive. From the 1960's to the 1980's, various $K^-p \rightarrow$ meson-baryon, e.g., K^-p , K^0n , $\pi\Lambda$, $\pi\Sigma$, and so on, scattering data were measured on a hydrogen target using bubble chambers to study the $\bar{K}N$ interaction [8–12]. This method of course did not allow access below the $\bar{K}N$ mass threshold and measurements in the low momentum region were difficult and data were insufficient. Nevertheless, the value of the $\bar{K}N$ interaction at the $\bar{K}N$ mass threshold was obtained by extrapolating it from the high momentum region, where abundant data exist, using several models [13–16]. These values are shown in Figure 1.1 as the characteristic X-ray values for kaonic hydrogen, discussed below. Due to the lack of data in the low

momentum region, these values varied. However, they were all attractive and consistent with the $\Lambda(1405)$ being a $\bar{K}N$ bound state.

An attempt to measure $\bar{K}N$ interactions at the $\bar{K}N$ mass threshold using kaonic hydrogen has been proposed. In this method, a K^- meson beam is stopped in a hydrogen target, and the characteristic X -rays emitted when the kaon binds to a proton are utilized. In the case of nucleon-meson, the characteristic X -ray is affected not only by electromagnetic interactions but also by the strong interactions i.e. $\bar{K}N$ interaction, leading to a shift in energy and a gain in width compared to the case where only electromagnetic interactions are present. According to Deser-Trueman formula [36, 37], these shift and width are model-independent and given by $\Delta E_1^s - \frac{i}{2}\Gamma_1 = -2\alpha^3\mu_c^2 a_{K-p}$. Where α is the fine structure constant, μ_c is the mass of the K^-p system, and a_{K-p} is the scattering length of the $\bar{K}N$ interaction. Several attempts were made in the 1980s using liquid hydrogen targets [17–19]., but the results showed a positive energy shift, indicating that the $\bar{K}N$ interaction is repulsive, contradicting $\bar{K}N$ scattering experiments. To improve the poor signal-to-noise ratio of these experiments, experiments were conducted at KEK PS using gaseous hydrogen targets, and a negative energy shift was reported, thus confirming that the $\bar{K}N$ interaction is attractive [20].

Once the $\bar{K}N$ scattering experiments and characteristic X -ray measurements were found to be qualitatively consistent, this led to further investigations into the $\bar{K}N$ interaction. The scattering length from characteristic X -ray measurements was determined more precisely by DEAR [35] and the SIDDHARTA Collaboration [21]. The values of these experiments are also shown in Figure 1.1. The SIDDHARTA data serve as a crucial constraint on the $\bar{K}N$ mass threshold, playing a key role in constraining the $\bar{K}N$ scattering amplitudes discussed later.

1.3 Two pole strcture of the $\Lambda(1405)$

A theoretical extrapolation of the $\bar{K}N$ scattering amplitude to the low-momentum regime was made in an effort to better understand the low-energy behavior. However, applying a low-momentum perturbation expansion to the strangeness sector proved to be challenging due to the presence of $\Lambda(1405)$.

This model suggested that $\Lambda(1405)$ receives contributions from two poles [27]: one being a bound state located in the high-mass region of the $\bar{K}N$ system at $1426 + 16i$ MeV, and the other being a resonant state of the $\pi\Sigma$

system located in the low-mass region at $1390 + 66i$ MeV. Due to contributions from both poles, the spectral shape and intensity of $\Lambda(1405)$ are expected to depend on the reaction mechanism and the $\pi\Sigma$ decay modes. Therefore, it is important to collect data on various $\pi\Sigma$ modes through the use of different reaction mechanisms.

1.4 Recent experimental status of the $\Lambda(1405)$

Experiments using two reaction mechanisms were conducted in this context. One is photoproduction, $\gamma p \rightarrow K^+ \Lambda(1405)$, and the other is proton-proton collisions, $pp \rightarrow nK^+ \Lambda(1405)$.

The photoproduction experiment was first performed at LEPS using a 1.5-2.4 GeV γ -ray beam, where the $\pi^-\Sigma^+$ and $\pi^+\Sigma^-$ spectra were reported [23]. The difference between these two spectra was attributed to the interference between the $I = 0$ and $I = 1$ components, and this interference term was observed. Subsequently, the CLAS Collaboration reported the spectra of all three $\pi\Sigma$ modes, i.e., $\pi^-\Sigma^+$, $\pi^+\Sigma^-$ and $\pi^0\Sigma^0$, using 1.61-1.91 GeV γ -ray beams, and all three spectral shapes were different [24]. They also experimentally confirmed that $\Lambda(1405)$ has isospin $I = 0$ and spin-parity $I^P = (\frac{1}{2}^-)$ [25]. Those three spectra were reproduced by theoretical calculations of the photoproduction process using the chiral unitary model [26]. However, in these calculations, some phenomenological parameters were adjusted by fitting the spectra, indicating that the photoproduction process is complex and that it is not possible to conclude how the $\Lambda(1405)$ poles affect the spectra.

Results from proton-proton scattering were reported by the HADES collaboration using proton beam with 3.5 GeV, which presented spectra of $\pi^-\Sigma^+$ and $\pi^+\Sigma^-$ [28]. Differences were observed in these spectra, indicating that $I = 0$ and $I = 1$ interference was also present in proton-proton scattering. The peaks of these two spectra are clearly located below 1400 MeV, indicating that the peak position of $\Lambda(1405)$ strongly depends on the production mechanism. However, as in the case of photoproduction, the production mechanism of $\Lambda(1405)$ in proton-proton scattering is complex, and it is not possible to conclude how its poles affect the spectrum.

1.5 Recent theoretical status of the $\Lambda(1405)$

Although the various experiments described above do not provide conclusive information on the poles of $\Lambda(1405)$, they play an important role in

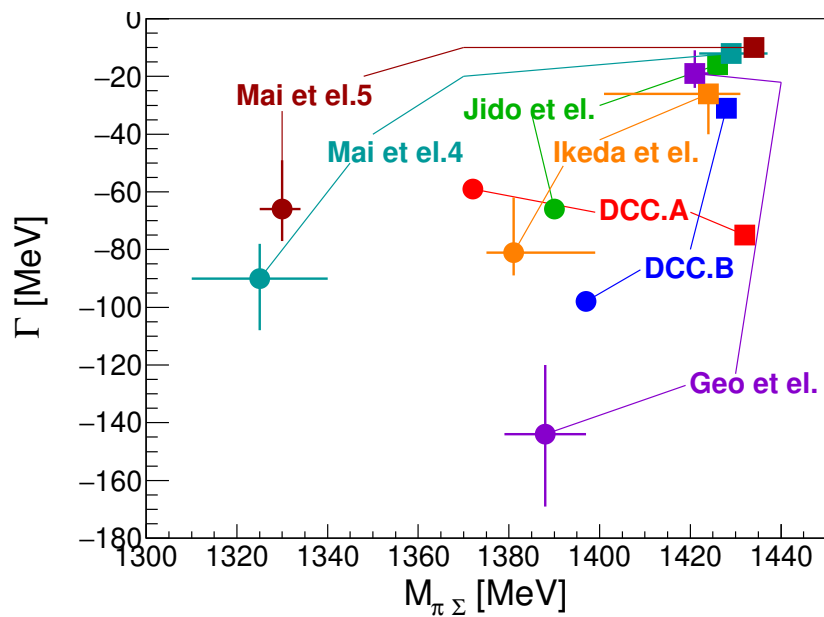


Figure 1.2: This figure shows the pole structure with $I = 0 \bar{K}N$ scattering amplitudes below the $\bar{K}N$ threshold by various theoretical analysis.

theoretical studies. Building on these results, theoretical studies based on the chiral unitary model have aimed to obtain more detailed $\bar{K}N$ scattering amplitudes while imposing chiral symmetry and unitarity conditions.

Y. Ikeda et al. [29] and Z.-H. Geo et al. [30] theoretically calculated the $\bar{K}N$ scattering amplitudes by incorporating not only the results of $\bar{K}N$ scattering experiments but also the SIDDARTA experimental results as constraints, including not only the leading order but also the next-to-leading (NLO) order in their analysis. M. Mai et al. derived several solutions through a similar analysis and tested them against the results of the CLAS experiment [31]. However, since the CLAS experimental data require reaction-specific calculations for fitting, they could not be directly incorporated into the fitting procedure. Instead, they were used as a filter to evaluate the resulting solutions, leaving two viable candidates.

Since chiral unitary calculations are based on perturbative expansions at low momentum, low-momentum $\bar{K}N$ scattering data have been primarily used. However, due to experimental difficulties, the available low-momentum data are insufficient, whereas medium- to high-momentum scattering data are more abundant. Partial wave analysis is known as a method applicable to this energy region and has been extensively studied, as described in Section 1.2. It continues to evolve with the incorporation of new data [32, 33]. However, even with this approach, drawing conclusions at low momentum has been difficult due to the presence of $\Lambda(1405)$. To overcome this challenge, the $\bar{K}N$ scattering amplitudes analyzed using the DCC model, a dynamic extension of partial wave analysis, were reported [34]. The analysis produced two solutions for the scattering amplitudes, primarily due to the lack of data in the low-momentum region. Although both scattering amplitudes exhibit two poles in the S -wave scattering below the $\bar{K}N$ mass threshold, similar to the chiral unitary model, the parameters of these poles were very different. The pole positions of $\Lambda(1405)$ based on the theoretical analysis presented in this chapter are summarized in Figure 1.2.

1.6 $d(K^-, n)$ reaction

Given the aforementioned circumstances, it is strongly desired to measure direct $\bar{K}N$ scattering data in the mass region of $\Lambda(1405)$. However, if the scattered \bar{K} meson and nucleon are detected as free particles after $\bar{K}N$ scattering, scattering amplitudes below the $\bar{K}N$ mass threshold cannot be obtained. As stated in Section 1.2, while the $K^- p$ reaction provides scattering data above the $\bar{K}N$ mass threshold, it cannot provide scattering amplitudes

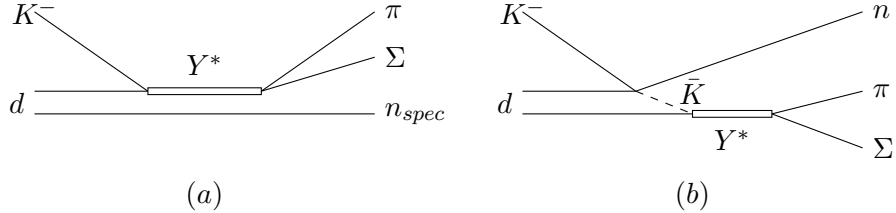


Figure 1.3: This figure is a diagram of the $K^-d \rightarrow n\Sigma\pi$ reaction. The left figure (a) represents a one-nucleon reaction, and the right figure (b) represents a two-step reaction.

below the threshold due to energy conservation. Thus, the $K^-d \rightarrow nY^*$ reaction with a deuterium target can be used, in which Y^* can be produced below the $\bar{K}N$ mass threshold by transferring the energy of the K^- beam to the neutron.

Experiments using this reaction were conducted at CERN by irradiating a liquid deuterium target with a K^- beam having a momentum of 686-844 MeV/c [38]. Although only the spectrum of the $\pi^+\Sigma^-$ mode was reported in this experiment, the spectrum showed a peak around 1420 MeV, which is higher than the conventional peak position of $\Lambda(1405)$. Since this reaction is \bar{K} -induced, it is considered to strongly reflect the $\bar{K}N$ pole, which is consistent with the chiral unitary model. In fact, D. Jido et al. used the chiral unitary model to calculate the $K^-d \rightarrow n\Sigma\pi$ reaction and successfully reproduced the experimental spectrum [39]. However, their calculation also required the P -wave $\Sigma(1385)$ contribution at $I = 1$. The $\pi\Sigma$ spectrum is reported only for $\pi^+\Sigma^-$ in this experiment, but a $\pi^-\Lambda$ spectrum from the $K^-d \rightarrow p\Lambda\pi^-$ reaction was also reported. Since this spectrum corresponds to $I = 1$, it does not include a $\Lambda(1405)$ contribution but does contain a $\Sigma(1385)$ contribution. J. Yamagata et al. reproduced the $\pi^-\Lambda$ spectrum of this experiment using the same reaction calculation framework [40]. Thus, this experiment provides strong support for the validity of the chiral unitary model.

Two types of reactions are possible for this process: a one-nucleon reaction (a) and a two-step reaction (b), as shown in Figure 1.3. These two reactions are kinematically distinguishable, but not in this experiment, where all Y^* production angles were measured. Nevertheless, neutrons originating from Fermi motion, which do not contribute directly to the reaction, are emitted in all directions. Therefore, the one-nucleon reaction is considered to play a more significant contribution in this experiment.

Summarized, only the $\pi^-\Sigma^+$ spectrum was reported in this experiment, and the reaction mechanism remained unknown. The J-PARC E31 experiment was planned to address this issue.

1.7 The J-PARC E31 experiment

The J-PARC E31 experiment employs a two-step reaction, as shown in Figure 1.3-(b). In this reaction, the irradiated K^- beam knocks out a nucleon in deuterium, which are then scattered forward. In addition, a Cylindrical Detector System (CDS) is installed around the liquid deuterium target to identify the $\pi\Sigma$ decay mode, and the particles originating from the decay of the produced Y^* will be measured. In this experiment, a 1 GeV/c K^- beam is used, which frequently undergoes $K^-N \rightarrow \bar{K}N$ elastic scattering. When the missing mass of Y^* produced in this reaction is near the $\bar{K}N$ threshold, the momentum of the scattered \bar{K} is around 250 MeV/c, making it easier to induce a secondary reaction with the residual nucleon.

In this experiment, all $\pi\Sigma$ modes are measured, i.e., the $\pi^-\Sigma^+$, $\pi^0\Sigma^0$, and $\pi^+\Sigma^-$ spectra. However, this paper focuses on discussing the $\pi^-\Sigma^+$ and $\pi^+\Sigma^-$ spectra. These spectra include contributions from $I = 0$ and $I = 1$ states, and their interference terms. However, using only these two spectra, it is impossible to fully disentangle the individual contributions. Therefore, we also discuss the $K^-d \rightarrow p\pi^-\Sigma^0$ spectrum, in which the proton is detected in the forward direction. This spectrum is purely associated with $I = 1$, and by incorporating this information, the $I = 0$, $I = 1$, and interference component can be fully disentangled.

One such calculation was performed by Miyagawa et al [42]. They used the scattering amplitudes from the latest partial-wave analysis for the first-step $\bar{K}N \rightarrow \bar{K}N$ scattering and those from some chiral unitary approaches for the second-step $\bar{K}N \rightarrow \pi\Sigma$ scattering. Thus, their calculation adopts a *hybrid* method that combines two different approaches. This is because the chiral unitary approach is specialized for low-energy interactions and is not applicable to the first-step $\bar{K}N \rightarrow \bar{K}N$ scattering. The spectrum of this experiment, considering the same two-step scattering process, has also been calculated using the DCC model. As mentioned in Section 1.5, this model extends the partial-wave analysis, which had been difficult to apply to the $\Lambda(1405)$ region, thereby making it applicable to that region.

The setup for this experiment, briefly introduced at the beginning of this chapter, is detailed in Chapter 2. The calibration and analysis methods for the detectors are described in Chapter 3. The selection of $\pi\Sigma$ modes from the

measured data and their conversion to cross sections are described in Chapter 4. The physical interpretation of the obtained spectra is discussed in Chapter 5. There, we discuss how well $\bar{K}N$ scattering is understood by comparing it with the theoretical calculations presented in this chapter, especially in the region of $\Lambda(1405)$. In doing so, we examine the contribution of each component by decomposing it into $I = 0$, $I = 1$, and their interference terms. Finally, using the $I = 0$ spectrum obtained from this experiment, we determine its scattering length and effective range, from which we derive the pole parameters of $\Lambda(1405)$, namely its mass and width.

Chapter 2

Experimental setup

Chapter 3

Analysis

Chapter 4

$\pi\Sigma$ Spectra

4.1 Decomposition of the $K^-d \rightarrow n\pi^+\pi^-n$ events

4.1.1 Backward $\pi^\mp\Sigma^\pm$ event selection

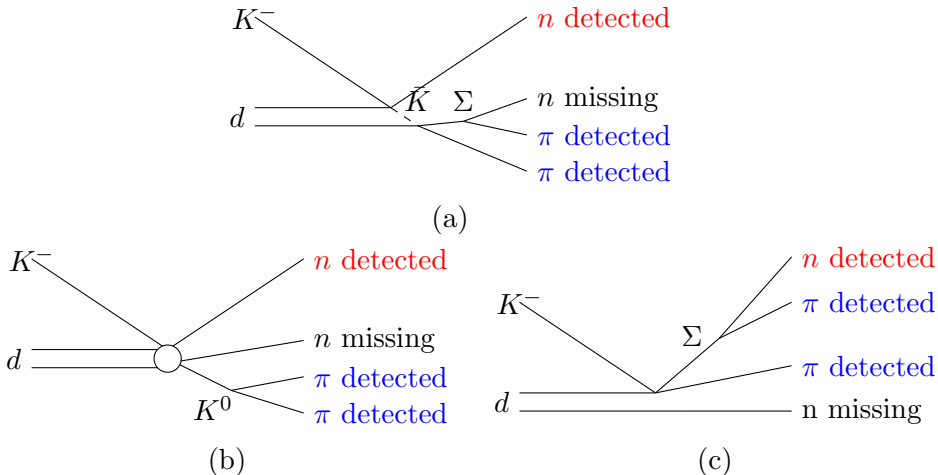


Figure 4.1: These figures illustrate the reaction diagrams of this final state. (a) shows backward $\pi\Sigma$ scattering via virtual \bar{K} ; (b) depicts direct decay from real K^0 to $\pi^+\pi^-$; (c) indicates forward Σ production. Colored particles indicate that a particle was detected. Red and blue mean detection by the NC and the CDS, respectively.

The $K^-n \rightarrow n\pi^+\pi^-n$ final state is identified from the event in which the forward neutron is detected, as described in Section.???. This final state can

be considered to include the three reactions represented in Figure 4.1. The first is the signal reaction in this analysis where \bar{K} is recoiled backward to $\pi\Sigma$ as shown in Figure 4.1-(a), the second is the recoil of K^0 decaying directly to $\pi^+\pi^-$ as shown in Figure 4.1-(b), and the third is the forward production of Σ ($\Sigma_{forward}$) as shown in Figure 4.1-(c), where forward means that the n decaying from Σ are detected by the NC. Reactions (b) and (c) can be identified by reconstructing K^0 and Σ^\pm from the invariant masses of π^+ and π^- and forward neutrons and π^\pm , respectively, as shown in Figure 4.2. The invariant mass distributions of $\pi^+\pi^-$, $n\pi^-$ and $n\pi^+$ are represented in the right, center and left figures respectively. For the identification of K^0 and $\Sigma_{forward}^\pm$, fitting with third-order polynomial function and Gaussian function is used to identify K^0 and $\Sigma_{forward}^\pm$ in the 3σ region of the Gaussian function, which is indicated by the red hatched area.

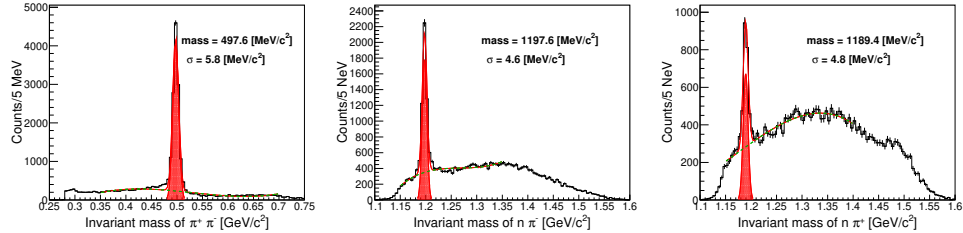


Figure 4.2: These figures show the invariant mass distributions of $\pi^+\pi^-$, $n\pi^-$ and $n\pi^+$ in the $Kd \rightarrow n\pi^+\pi^-n$ event sample from left to right. The Gaussian functions and the selection regions for K^0 and $\Sigma_{forward}^\pm$ are indicated by red hatched area. The background third-order polynomial functions are shown as the green dashed lines.

Rejecting these two reactions leaves a signal reaction in which $\pi\Sigma$ is scattered backward. This reaction has $\pi^-\Sigma^+$ and $\pi^+\Sigma^-$ modes, and they must be separated. The branching ratio of these modes depends on the mass of $\pi\Sigma$, and this separation is performed for each bin of $d(K^-, n)$ missing mass.

Figure 4.3 shows the $d(K^-, n)$ missing masses in which the $K^-d \rightarrow n\pi^+\pi^-n$ final state has been identified. On the left, all events, those identifying K^0 , those identifying $\Sigma_{forward}^+$, and those identifying $\Sigma_{forward}^-$ are indicated by black, green, red, and blue lines, respectively. The right figure shows the signal spectrum, subtracting the events identified as K^0 or $\Sigma_{forward}^\pm$ from all events.

To separate these events, we generated template events using a Geant4 Monte Carlo simulation and decomposed the reactions by fitting their spec-

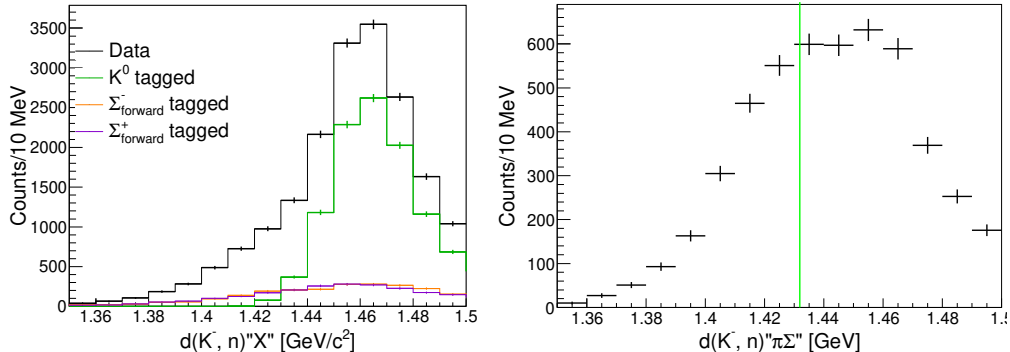


Figure 4.3: This figure shows the $d(K - n)$ spectrum of the $K^-d \rightarrow n\pi^+\pi^-n$ final state. The left figure shows the entire event sample of $K^-d \rightarrow n\pi^+\pi^-n$. The black, green, purple, and orange lines represent all events, events with identified K^0 , Σ^+ , and Σ^- , respectively. The right figure shows the signal events of backward-scattered $\pi\Sigma$, excluding those identified as K^0 or Σ^+/Σ^- .

tra with templates. This decomposition was applied not only to the signal but also to the background reactions. The procedures used in this decomposition are described in detail in Section 4.1.2. The estimation of the detector resolution used in this simulation is described in detail in Appendix B.

4.1.2 Template fitting

This subsection describes template fitting for reaction decomposition. As mentioned earlier, three possible reactions in the $K^-d \rightarrow n\pi^+\pi^-n$ final state were mentioned. Among them, backward $\pi\Sigma$ scattering (Figure 4.1-(a)) and forward $\pi\Sigma$ production (Figure 4.1-(c)) can be divided into two categories depending on the charge state of $\pi\Sigma$. In other words, template events were generated for the following five reactions:

1. $K^-d \rightarrow n_{forward}\pi^-\Sigma^+$ (Signal-1)
2. $K^-d \rightarrow n_{forward}\pi^+\Sigma^-$ (Signal-2)
3. $K^-d \rightarrow nK^0n$ (K^0 production)
4. $K^-d \rightarrow \Sigma^+\pi^-n$ ($\Sigma^+_{forward}$ production)
5. $K^-d \rightarrow \Sigma^-\pi^+n$ ($\Sigma^-_{forward}$ production)

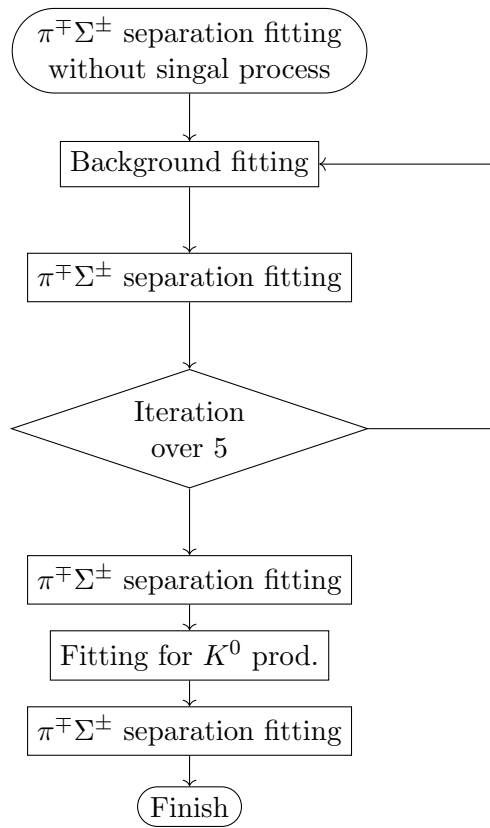


Figure 4.4: Flow chart of template fittings of this analysis.

Among these, reaction 3 is considered an elementary process in which the K^- strikes the proton in the deuteron, converting it into a neutron that is emitted forward, while the K^- itself recoils backward as a K^0 . In this reaction, the remaining nucleon acts as a spectator with Fermi momentum. The Fermi momentum is simulated using the results of the $d(e, e'p)n$ reaction [64]. In reactions 4 and 5, the Σ is scattered forward, and these are also regarded as elementary processes because a large portion of the K^- beam momentum is transferred to the Σ and the π . Extensive data on such elementary processes have been collected from scattering experiments using hydrogen targets, and their angular distributions are summarized in [63].

These three reactions are considered the background in this analysis, and template events need to be generated for backward $\pi\Sigma$ scattering (reactions 1 and 2), which represent the signal. However, no experimental data are available for these reactions, as they are two-step processes involving a virtual intermediate \bar{K} particle. Moreover, the fitting to separate the $\pi^-\Sigma^+$ and $\pi^+\Sigma^-$ modes is performed in each bin of the $d(K^-, n)\pi\Sigma$ missing mass. Additionally, these Monte Carlo samples are also used for acceptance correction, as described in Section 4.2. Therefore, the template events were generated assuming a uniform $\pi\Sigma$ mass distribution. The second-step scattering, $\bar{K}N \rightarrow \pi\Sigma$, was generated isotropically, assuming S-wave dominance of $\Lambda(1405)$.

Template fitting consists of two tasks: background estimation and the separation of the $\pi^-\Sigma^+$ and $\pi^+\Sigma^-$ modes. Background estimation is performed using all $K^-d \rightarrow n\pi^+\pi^-n$ final state events. In contrast, the separation of the charged modes is carried out using events from which background contributions (such as K^0 and *Sigma_{forward}* production) have been removed. These events are further divided into bins of the $d(K^-, n)\pi\Sigma$ missing mass. In other words, these two fittings cannot be performed simultaneously, as they use different event samples. Thus, the fitting procedure is conducted as illustrated in Figure 4.4.

First, an initial fit for $\pi^\mp\Sigma^\pm$ separation is performed without considering the background contributions. Next, a background fit is conducted to estimate the contribution from $\pi^\mp\Sigma^\pm$. Then, a fit for charge mode separation is carried out, taking background leakage into account. These fitting steps are iterated five times, as the background and $\pi\Sigma$ spectra influence each other.

Since it was found that the background of K^0 production includes reactions that are not elementary processes, a final fit is performed using K^0 -selected events to separate these contributions. This step is referred to as "Fitting for K^0 production" in Figure 4.4 and is described in detail in Appendix C. The final spectrum is obtained by performing one last fit for the

$\pi^\pm\Sigma^\pm$ charge mode separation. In this fitting, the background is removed within a 3σ , meaning that the “fitting for K^0 production” has almost no effect on the final result. These so-called template fittings are performed using ROOT’s TFractionFitter, which is implemented based on “Fitting with Finite Monte Carlo Samples” [66].

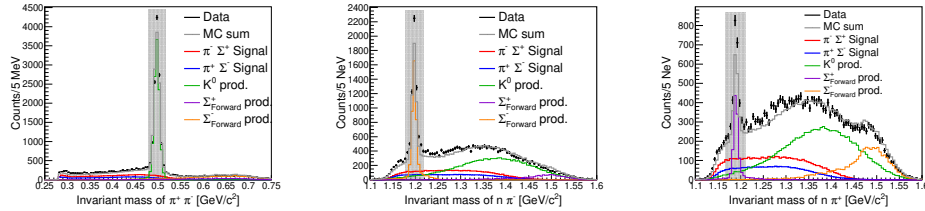


Figure 4.5: The figures show template fitting for background estimation. The right, center, and left figures show invariant masses of $\pi^+\pi^-$, $n\pi^-$ and $n\pi^+$, respectively. Error bars represent data spectra. Bold lines indicate the backward $\pi\Sigma$ production signals: red for $\pi^-\Sigma^+$ and blue for $\pi^+\Sigma^-$. Thin green, purple, and orange lines represent the K^0 , $\Sigma_{forward}^-$ and $\Sigma_{forward}^+$ production reactions. Gray lines show the sum of the Monte Carlo simulations. Gray hatched areas indicate the 3σ rejection regions estimated by fitting with a Gaussian function and a polynomial background.

Next, the fitting procedure for background estimation and $\pi^\pm\Sigma^\pm$ separation is explained in detail. Background fitting is performed using the invariant mass spectra of $\pi^+\pi^-$, $n_{forward}\pi^+$, and $n_{forward}\pi^-$ from all $K^-d \rightarrow n\pi^+\pi^-n$ final states shown in Figure 4.2. The contributions from each process, scaled according to the fitting results, are presented in Figure 4.5. K^0 , Σ^+ , and Σ^- production are represented by green, purple, and orange lines, respectively, and produce peaks at the corresponding $\pi^+\pi^-$, $n_{forward}\pi^+$, and $n_{forward}\pi^-$ invariant masses. The backward $\pi^-\Sigma^+$ and $\pi^+\Sigma^-$ scattering signals are shown in red and blue lines, respectively, and are uniformly distributed without peaks at these invariant masses.

The fact that these invariant mass distributions are reproduced using templates generated by the Monte Carlo simulation indicates that the $K^-d \rightarrow n\pi^+\pi^-n$ final state can be decomposed into the signal and K^0 and $\Sigma_{forward}^\pm$ production components. In template fitting, it is known that $-2\ln(\Lambda)$ asymptotically approaches χ^2 in the limit of an infinite number of samples, where Λ denotes the likelihood. In this fitting, $-2\ln(\Lambda)/NDF \sim \chi^2/NDF = 1077.4/352 = 3.06$.

Next, we explain the fitting procedure used to separate the $\pi^-\Sigma^+$ and $\pi^+\Sigma^-$ charge modes of the backward $\pi\Sigma$ scattering, which serves as the

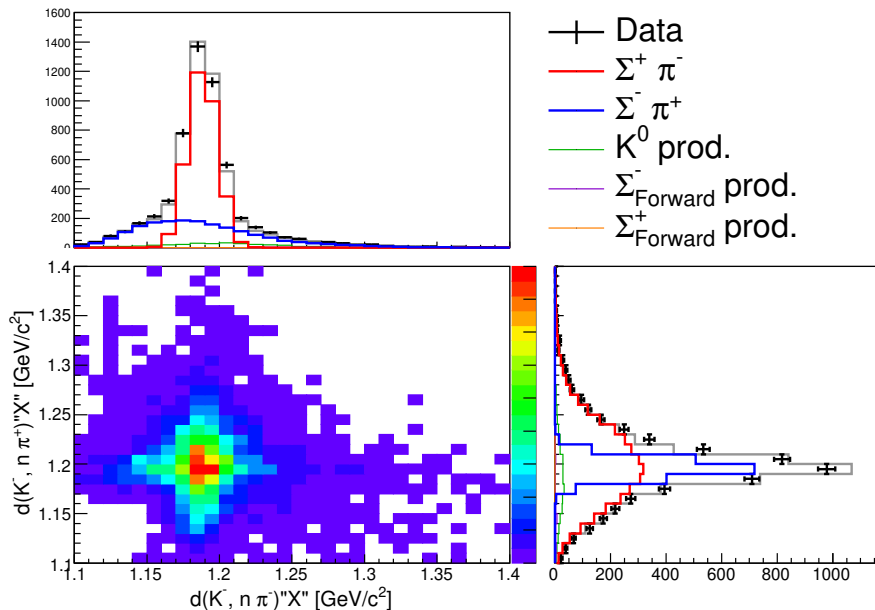
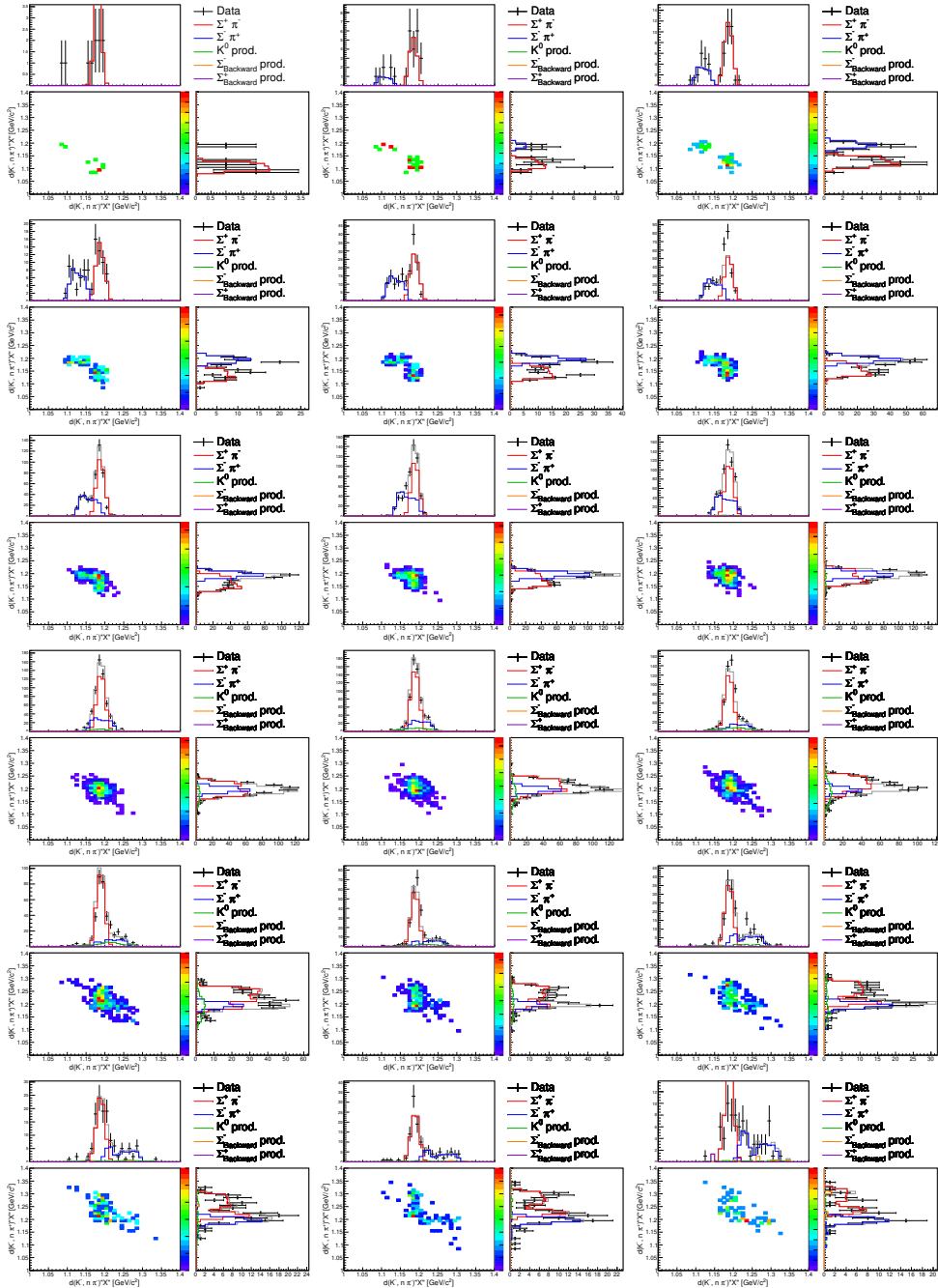


Figure 4.6: This figure shows template fitting of the $d(K^-, n\pi)$ spectra to separate the $\pi^-\Sigma^+$ and $\pi^+\Sigma^-$ modes. The lower left figure shows two-dimensional plots of $d(K^-, n\pi^-)$ and $d(K^-, n\pi^+)$ on the horizontal and vertical axes, respectively. The top and right panels show the projections onto each axis. The caption is the same as that of Figure 4.5.



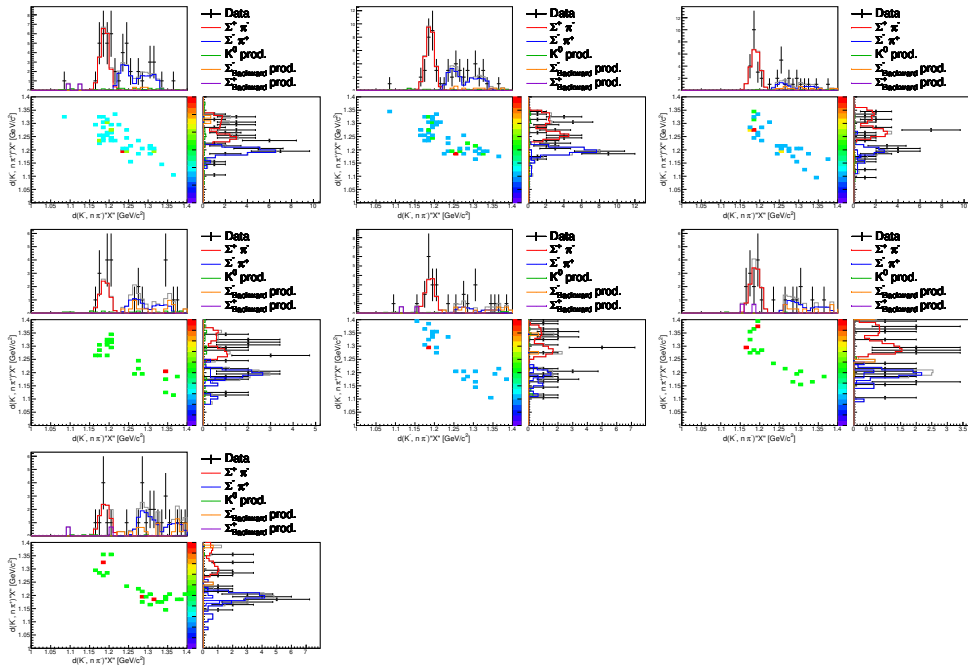


Figure 4.7: These figures are shown separately for each bin of $d(K^-, n)$ for fitting to separate $\pi^-\Sigma^+$ and $\pi^+\Sigma^-$ modes. The top left panel corresponds to the lowest missing mass bin (1.35-1.36 GeV), and each subsequent bin is shown to the right. That is, each row represents a 0.03 GeV range, covering the overall range from 1.35 to 1.60 GeV.

signal in this analysis. To this end, we use the missing masses of $d(K^-, n\pi^-)$ and $d(K^-, n\pi^+)$, obtained from events in the $K^-d \rightarrow n\pi^+\pi^-n$ final state after excluding background contributions from K^0 and $\Sigma_{forward}^\pm$ production, as shown in Figure 4.6. The lower left panel shows a two-dimensional plot of $d(K^-, n\pi^+)$ versus $d(K^-, n\pi^-)$ while the top and left panels display the one-dimensional spectra of the respective projections. These one-dimensional spectra were used for the fitting. This figure represents the summed fitting results over all bins of $d(K^-, n)\pi\Sigma$, and the individual figures for each bin are presented in Figure 4.7. The notations in the figure are consistent with those used for background fitting (Figure 4.5).

The background, represented by the green, purple, and orange lines, is removed within the 3σ region, resulting in minimal leakage, although it is still accounted for. The signal, such as the red line indicating the $\pi^-\Sigma^+$ mode, creates a peak in the $d(K^-, n\pi^-)$ missing mass (top panel) consistent with the missing Σ , whereas the $d(K^-, n\pi^+)$ missing mass (right panel) for the opposite charge does not form a peak but rather shows a broad distribution. The opposite charge mode, $\pi^+\Sigma^-$, exhibits similar behavior when the charge is reversed.

The values of $-2\ln(\Lambda)/NDF \sim \chi^2/NDF$ for each bin of $d(K^-, n)\pi\Sigma$ are shown in Figure 4.8. These fittings yield the $\pi^-\Sigma^+$ and $\pi^+\Sigma^-$ spectra shown in Figure 4.9, which are converted to the double-differential cross section by applying luminosity after acceptance correction, as described in the next subsection.

4.2 Conversion to the cross section

4.2.1 Acceptance correction

This section describes the CDS acceptance correction. For this correction, we use Monte Carlo simulation data for the $K^-d \rightarrow n\Lambda(1405)$, assuming a 2-step process, which was also used for the template fitting in the previous section. The CDS acceptance correction is applied not only to $d(K^-, n)\Lambda(1405)$ but also to $d(K^-, p)\Sigma^*$. The simulation data for this correction were generated in the same way as for the $K^-d \rightarrow n\Lambda(1405)$ reaction.

The forward-going neutrons (protons) are generated with a slightly wider angular distribution (± 8 degrees) than the acceptance of the forward detector system. However, since the purpose here is to estimate the CDS acceptance, only the events that are detected by the forward detector are considered as the sample population. Among these events, those that pass through the same analysis routine as the real data are regarded as valid events. In the

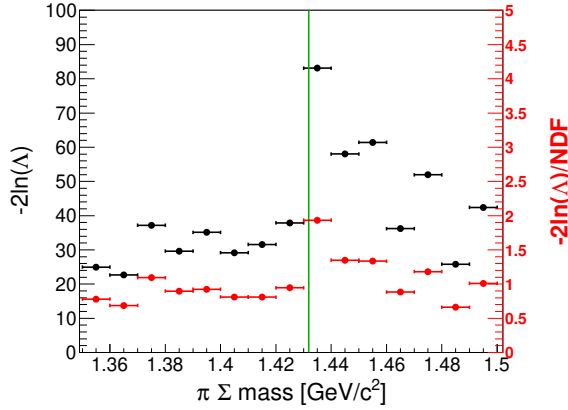


Figure 4.8: This figure shows the template fitting results of $-2\ln(\Lambda)$ and $-2\ln(\Lambda)/NDF$ for the separation of $\pi^-\Sigma^+$ and $\pi^+\Sigma^-$ modes in each $d(K^-, n)$ bin. Black and red lines indicate $-2\ln(\Lambda)$ and $-2\ln(\Lambda)/NDF$, respectively. The horizontal axis represents the (K^-, n) bin.

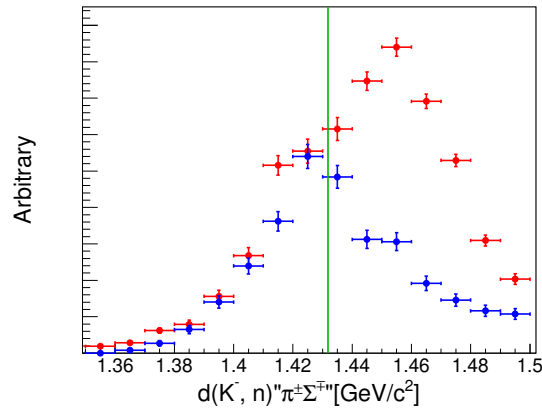


Figure 4.9: The $\pi^-\Sigma^+$ and $\pi^+\Sigma^-$ mode spectra obtained by template fitting are shown in arbitrary units. Red and blue lines indicate $\pi^-\Sigma^+$ and $\pi^+\Sigma^-$, respectively. The green vertical line is indicated the $\bar{K}N$ threshold.

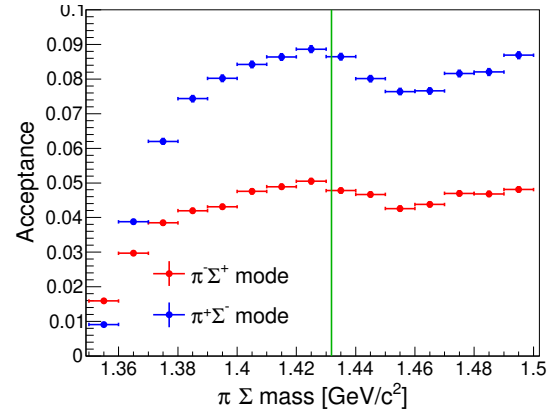


Figure 4.10: This figure shows the acceptance of $d(K^-, n)''\pi^+\Sigma^\pm$. The red line indicates $\pi^-\Sigma^+$ and the blue line indicates $\pi^+\Sigma^-$.

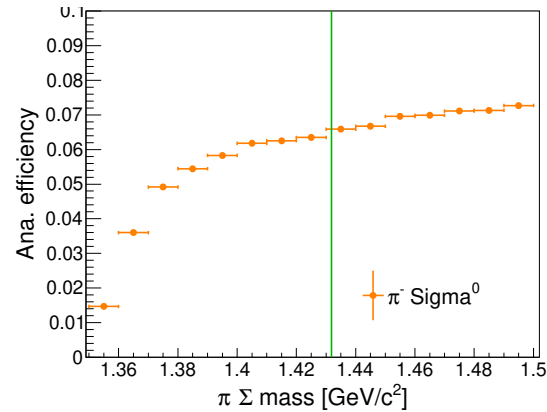


Figure 4.11: This figure shows $d(K^-, p)''\pi^-\Sigma^0$ acceptance

Table 4.1: Summary table of $d(K^-, n)$ scaling parameters

Component	value	error	value	error
Luminosity (/ μb)	5927	158		
Target Length (cm)			10	
Target density [g/cm^3]			$0.1613 - 0.1617$	0.0015
Number of Kaon			5.83×10^{10}	
Survival ratio of K^-			0.281	0.0003
DAQ live ratio			0.768	0.0021
Trigger efficiency				
$K \otimes CDH1$			0.9527	0.0004
Neutral			0.9992	6.7×10^{-6}
Efficiency of the CDC	0.977	0.04		
Efficiency of the NC	0.291	0.015		
Intrinsic the NC			0.317	0.016
Over veto of the CVC/BVC			0.081	0.007
Solid angle of the NC (msr)	21.5	0.2		

case of forward neutrons, the analysis includes events in which $\pi^+ \pi^-$ are detected, followed by the selection of $d(K^-, n\pi^+\pi^-)n$ events, and the rejection of K^0 and $\Sigma_{forward}^\pm$. In the case of forward protons, valid events are those in which $\pi^- \pi^-$ are detected, and are classified through the $d(K^-, p\pi^-\pi^-)\gamma p$ and $d(K^-, p\pi^-)\Lambda$ selections.

The CDS acceptances obtained for $d(K^-, n)\pi^\mp\Sigma^\pm$ and $d(K^-, p)\pi^-\Sigma^0$ are shown in Figures 4.10 and 4.11, respectively.

4.2.2 Conversion factors for the cross section

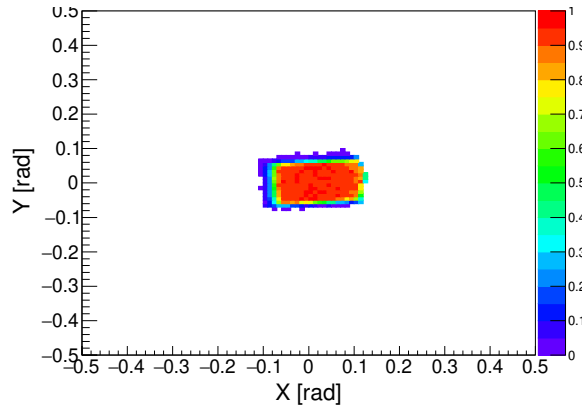
The factors for converting to double-differential cross sections are explained here. These can be categorized into the following three components:

1. Luminosity, which is determined by the number of incident beam particles and the number of target nuclei;
2. The solid angle and detection efficiency of the forward-scattered neutrons (or protons) produced in the reaction;
3. The detection efficiency of detectors.

These are summarized in Tables 4.1 and 4.2 for the forward neutron and forward proton cases, respectively.

Table 4.2: Summary table of $d(K^-, p)$ scaling parameters

Component	value	error	value	error
Luminosity ($/\mu b$)	2478	81		
Target Length (cm)			10	
Target density [g/cm^3]			0.1624	0.0014
Number of Kaon			2.05×10^{10}	
Survival ratio of K^-			0.336	0.0001
DAQ live ratio			0.821	0.0001
Trigger efficiency				
$K \otimes CDH1$			0.9527	0.0003
Charge			0.9559	0.0004
Efficiency of the CDC	0.977	0.04		
Efficeincy of the forward detectors	0.819	0.042		
Efficeincy of the FDC1	0.987	0.005		

Figure 4.12: This figure shows the effective rates of solid angle elements in the 1.44–1.45 GeV $\pi^- \Sigma^0$ mass bin, as estimated by Monte Carlo simulations.

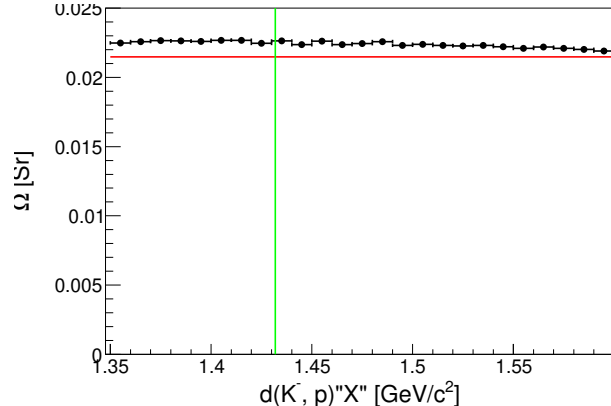


Figure 4.13: This figure shows the relationship between the mass of the $\pi^- \Sigma^0$ system and the solid angles of the forward detectors (FDC1 and PC/CVC) with respect to the outgoing forward proton. The red line indicates the solid angle of the NC detector with respect to the forward neutron.

Luminosity is a quantity that represents the product of the number of incident beam particles and the number of target particles. The beam intensity is evaluated by multiplying the beam scaler counts by the DAQ live ratio, described in Section ??, which accounts for the fraction of data actually recorded for analysis; the trigger efficiency, described in Section ??, which accounts for whether a trigger signal was actually generated; and the fraction of K^- beam triggers that passed through the fiducial volume of the target, as described in Section ???. This beam-related quantity is calculated and summed on a run-by-run basis. Tables 4.1 and 4.2 show representative values consisting of the average over all runs and the errors evaluated from the fluctuations. For the number of target particles, the density of the liquid deuterium target is estimated from the monitored temperatures, as described in Section ?? The uncertainty is evaluated based on fluctuations during the production run and is calculated by multiplying the density by the length of the fiducial volume.

In the case of forward neutrons, since they travel in straight trajectories, the solid angle can be defined by the area covered by the NC. When the solid angle is evaluated at the center of the NC and the variation is assessed by shifting the evaluation point front and back, it is determined to be 21.5 ± 0.2 [msr]%. The detection efficiency of the neutron detector can be divided into two components the intrinsic detection efficiency of the NC for neutrons and the over-veto effect by the CVC. The intrinsic neu-

tron detection efficiency is evaluated to be 31.7 ± 1.6 [%] using the reaction $K^- p \rightarrow K^0 n \rightarrow \pi^+ \pi^- n$ with a liquid hydrogen target, as described in Section ???. The over-veto effect in the CVC, which is also considered to be strongly influenced by beam-induced background, is evaluated to be 8.1 ± 0.7 [%] using the production run data, also described in Section ??.

In the case of forward protons, since they are bent by the Usniwaka magnet, the solid angle coverage depends on the momentum of the forward-scattered proton, i.e., the mass of the $\pi^- \Sigma^0$ system. To estimate this, we use a dataset similar to the Monte Carlo simulation used for the acceptance correction. The solid angle for a given $\pi^- \Sigma^0$ mass region is evaluated by dividing the angular space into small solid angle elements. For each element, the detection efficiency of the forward detector system (CVC/PC) is evaluated based on whether the proton can actually be detected. The effective solid angle for each element is then calculated by multiplying the element's solid angle by its detection efficiency, as shown in Figure 4.12. Finally, the total solid angle is obtained by summing these effective solid angles over all elements, as shown in Figure 4.13. The solid angle does not change significantly in the region of interest.

In this data set, hadronic reactions and similar processes that could cause secondary interactions are turned off to avoid double-counting losses already accounted for in the detection efficiency of forward protons evaluated in Section ???. Here, the detection efficiency of protons was estimated to be 81.9 ± 4.2 [%] using the $K^- d \rightarrow \pi^- \pi^- pp$ reaction. Also, the detection efficiency of FDC1 was evaluated to be 98.7 ± 0.5 [%] using the BVC as the trigger detector under the pion beam conditions, as described in Section ??.

After applying the CDS acceptance obtained in the previous subsection and the correction factors described here, we obtain the $d(K^-, n)\pi^\mp \Sigma^\pm$ and $d(K^-, p)\pi^- \Sigma^0$ cross sections, as shown in Figures 4.14 and 4.15, respectively.

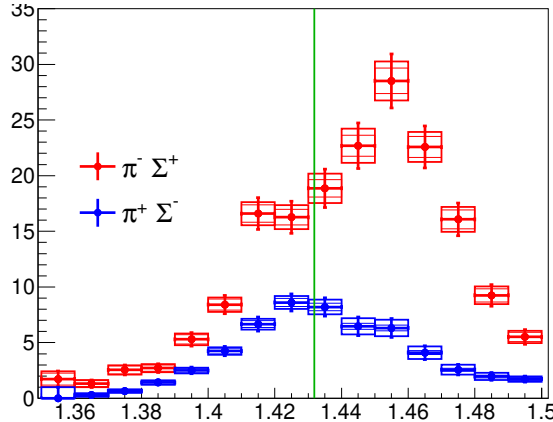


Figure 4.14: The red figure and blue figure shows about $d(K^-, n)''\pi^+\Sigma^-''$ and $d(K^-, n)''\pi^-\Sigma^+''$, respectively. The inner frame (thin line), outer frame (thick line), and error bars represent the addition of statistical errors, fitting errors, and conversion errors, which were calculated by root-mean-square. The green vertical lines indicates $\bar{K}N$ threshold.

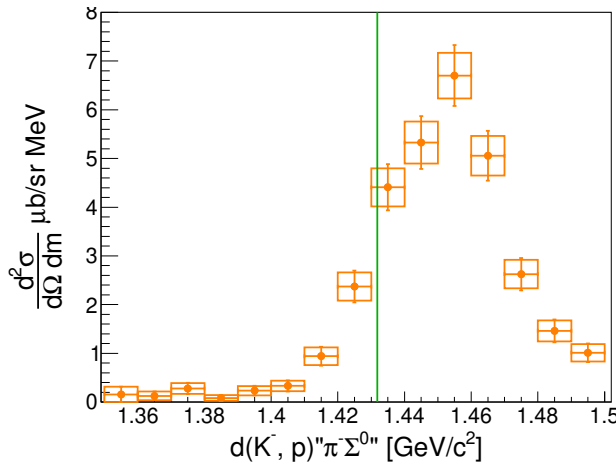


Figure 4.15: This figure shows the cross section of $d(K^-, p)''\pi^-\Sigma^0''$. The box represents the statistical error, and the error bar represents the root mean squares of the conversion factor added to it. The green vertical lines indicates $\bar{K}N$ threshold.

Chapter 5

Discussion

5.1 Spectra

5.1.1 Qualitative properties of obtained spectra

The $d(K^-, n)\pi^\mp\Sigma^\pm$ and $d(K^-, p)\pi^-\Sigma^0$ spectra obtained through the procedures described in the previous section are shown together in Figure 5.1. In this figure, the green vertical line indicates the $\bar{K}N$ threshold. This section discusses the qualitative features of the obtained spectra.

The experiment is interpreted as a two-step reaction, as described in Section 1.7. The $\pi^-\Sigma^0$ spectrum contains only the $I = 1$ component from the second-step scattering, and this second-step scattering does not exhibit a significant structure, as there is no pole near the $\bar{K}N$ threshold. As a result, the $\bar{K}N$ spectrum reflects the first-step scattering more directly. A bump-like shape emerges from the $\bar{K}N$ threshold due to the Fermi motion of the spectator.

For the $I = 0$ component, the second-step scattering is expected to exhibit a pronounced structure below the $\bar{K}N$ threshold due to the presence of poles in that region. This results in a spectral shape with a stronger enhancement below the $\bar{K}N$ threshold compared to the bump-like feature originating from the first-step scattering. Indeed, the observed $\pi^\mp\Sigma^\pm$ spectra, which contain both $I = 0$ and $I = 1$ components as well as their interference, exhibit a clear structure below the $\bar{K}N$ threshold. The overall spectral intensity is also larger than that of the $\pi^-\Sigma^0$ spectrum, which only contains the $I = 1$ component, due to the pole contribution in the $I = 0$ channel. The interference between the $I = 0$ and $I = 1$ components appears as a difference between the $\pi^-\Sigma^+$ and $\pi^+\Sigma^-$ spectra. Since the measured spectra show a clear asymmetry between them, the interference effect be-

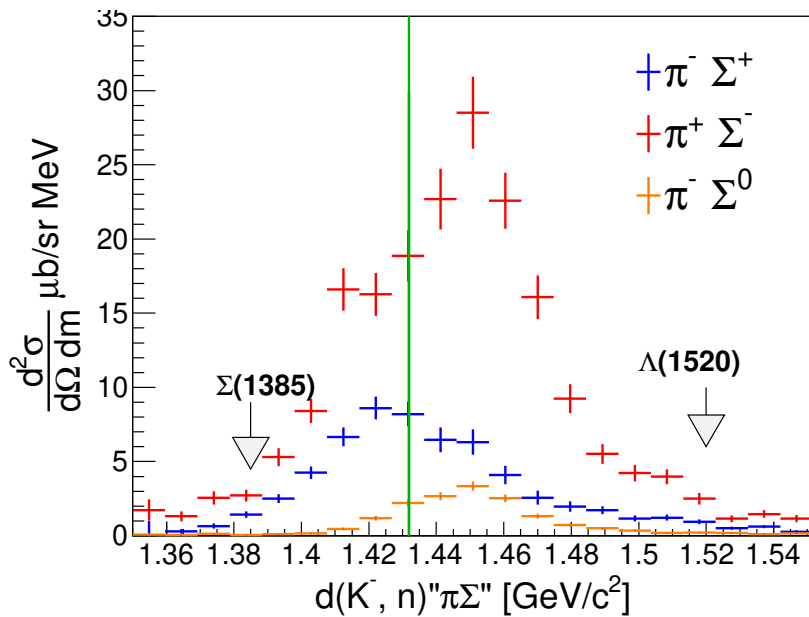


Figure 5.1: The obtained cross sections are plotted simultaneously in this figure. The $d(K^-, n)''\pi^-\Sigma^+$, $d(K^-, n)''\pi^+\Sigma^-$, $d(K^-, n)''nK^0''$, and $d(K^-, p)''\pi^-\Sigma^0''$ plot as red, blue, green, and orange, lines respectively. The $d(K^-, n)''nK^0''$ is scaled to 1/10. The green vertical line indicates the $\bar{K}N$ threshold.

tween $I = 0$ and $I = 1$ was observed in the reactions in this experiment.

In the second-step scattering near the $\bar{K}N$ threshold, S -waves are expected to dominate due to the small angular momentum transfer transfer. However, it is well known that in this region there are $I = 0$ D -wave resonances, such as the $\Lambda(1520)$, and $I = 1$ P -wave resonances, such as the $\Sigma(1385)$. The absence of structures around the $\Sigma(1385)$ region in the measured $I = 1 \pi^-\Sigma^0$ spectrum, as well as around both the $\Sigma(1385)$ and $\Lambda(1520)$ regions in the $\pi^+\Sigma^-$ and $\pi^-\Sigma^+$ spectra with mixed $I = 0$ and $I = 1$ contributions, confirms that the S -wave dominates in the reactions observed in this experiment.

5.1.2 Comparison with theoretical calculations

The previous section discussed the qualitative features of the obtained spectra. In this section, we examine how well the reaction can be understood by comparing the data with theoretical calculations that take into account the kinematics of this experiment.

Two theoretical calculations are used for this purpose. One is the *hybrid* calculation by Miyagawa et al., which separates the reaction into a first-step high-energy $K^-N \rightarrow \bar{K}N$ scattering and a second-step low-energy $\bar{K}N \rightarrow \pi\Sigma$ scattering, which is the main focus. In the second-step, three different scattering amplitudes obtained from various analyses of the $\Lambda(1405)$ are used. This is to say, this method allows the second-step scattering amplitudes to be substituted with results from any $\Lambda(1405)$ analysis. The other method is the DCC method, which treats these energy regions in a unified manner and uses continuous scattering amplitudes for both scatterings. In this method, there are two sets of datasets, A and B, with the main uncertainty due to the lack of scattering data in the low energy region.

Figure ?? shows a comparison between the experimental data and the predicted spectra from theoretical calculations. The theoretical spectra are convolved with the detector resolution described in Appendix ???. From top to bottom, the $\pi^+\Sigma^-$, $\pi^-\Sigma^+$, and $\pi^-\Sigma^0$ spectra are shown. The right column shows the results from the DCC method [46], and the left column shows those from the hybrid calculation by Miyagawa et al [42].

The spectral shapes calculated by the two theoretical methods reproduce well the qualitative features discussed in the previous section. Specifically, the $\pi^-\Sigma^0$ spectrum with an $I = 1$ contribution exhibits a bump structure reflecting the first-step scattering, while the $\pi^\mp\Sigma^\pm$ spectra, which include $I = 0$, $I = 1$, and their interference components, show a clear structure below the $\bar{K}N$ threshold. The difference observed between the $\pi^+\Sigma^-$ and

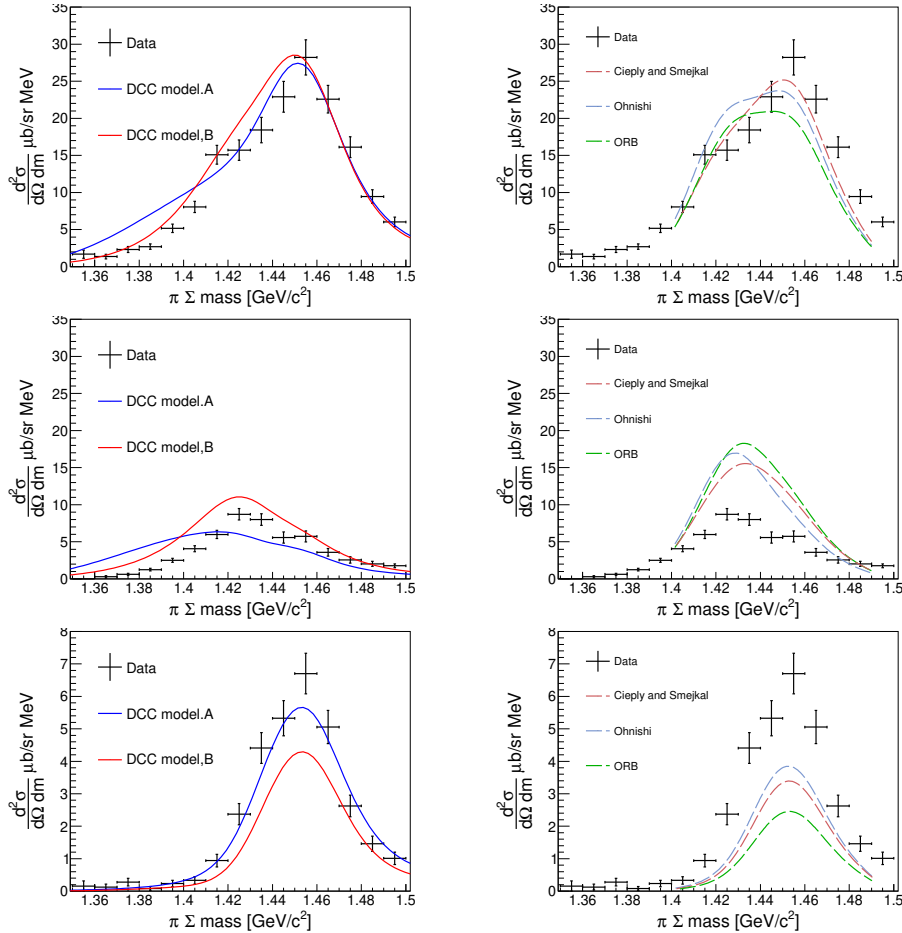


Figure 5.2: This figure shows a comparison of our obtained spectra with predictions from theoretical calculations. The top, middle, and bottom figures represent $\pi^-\Sigma^+$, $\pi^+\Sigma^-$, and $\pi^-\Sigma^0$, respectively. The right figure shows the spectrum predicted by the DCC model [46], and the left figure shows the spectrum predicted by the calculation of Miyagawa et al [42]. The spectra predicted by theoretical calculations are convoluted with our detector resolution.

$\pi^-\Sigma^+$ spectra, which originates from the interference between the $I = 0$ and $I = 1$ components, is also reasonably well reproduced by the calculations.

However, the spectra predicted by the DCC method are well reproduced, both in shape and intensity. In contrast, the hybrid calculation reasonably reproduces the $\pi^+\Sigma^-$ spectrum in both shape and intensity, but significantly overestimates the intensity of the $\pi^-\Sigma^+$ spectrum and underestimates that of the $\pi^-\Sigma^0$ spectrum.

This implies that a continuous treatment of the first- and second-step scattering is essential for understanding the present reaction. That is to say, consistency with the higher-energy region is important for understanding $\bar{K}N$ scattering in the $\Lambda(1405)$ region.

The following discussion focuses on the spectra calculated by the DCC method.

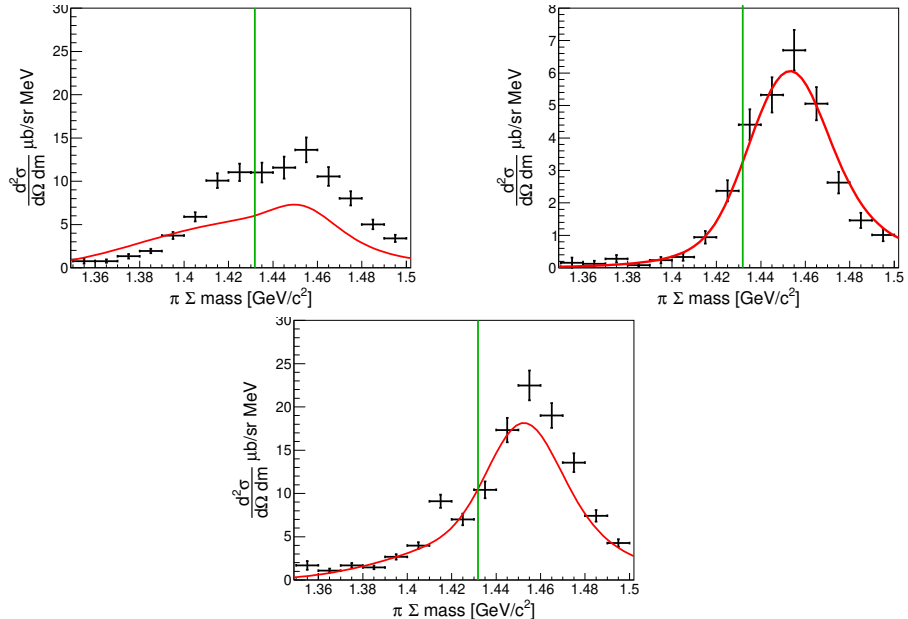


Figure 5.3: This figure illustrates the spectra of the experimental data, decomposed into $I = 0$, $I = 1$, their interference terms, and the corresponding fitting results obtained using Model A of the DCC model. The black error bars represent the experimental data, while the red line denotes the fit results. The upper-left panel corresponds to $I = 0$, the upper-right panel to $I = 1$, and the lower panel to the interference term.

The method described in the previous section focused solely on the $I = 0$

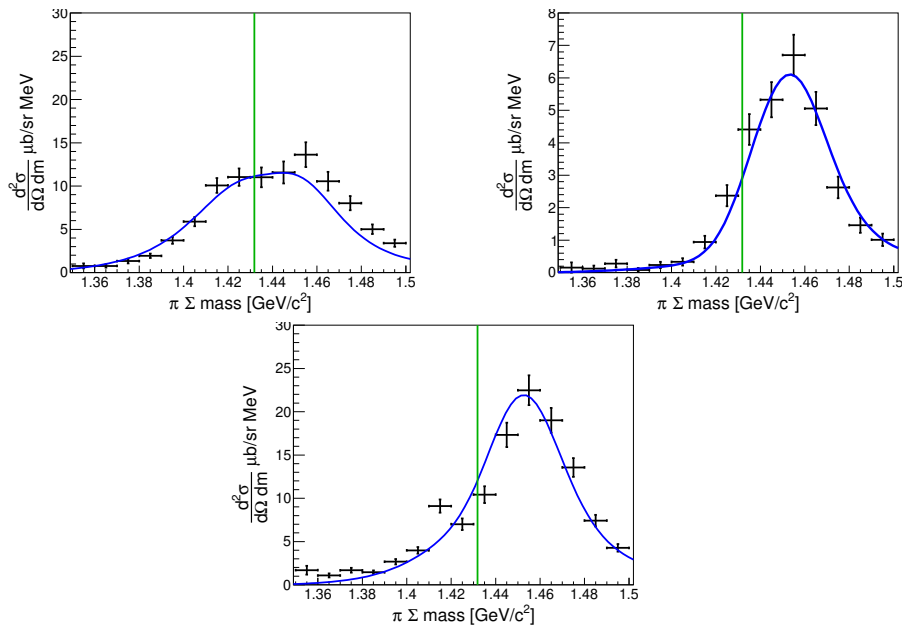


Figure 5.4: This figure presents the results of fitting the experimental data using Model B. The blue line represents the fit results, while other notations follow the same conventions as in Figure 5.3.

component, leaving $I = 1$ and the interplay between $I = 0$ and $I = 1$ in the obtained spectra unexplored. To address this limitation, we will utilize spectra derived from the DCC model to examine these contributions. First, we fit the experimental spectra we obtained by introducing the parameters $S_{I=0}$ and $S_{I=1}$, which adjust the strengths of $I = 0$ and $I = 1$ components independently. Two versions of the DCC model, Model A and Model B, are considered. Figures 5.3 and 5.4 correspond to cases using Model A and Model B, respectively. For the fitting performed with Model A, the parameter for $I = 0$ was reduced to $S_{I=0} = 0.562 \pm 0.015$, while the parameter for $I = 1$ remained nearly unchanged at $S_{I=1} = 1.070 \pm 0.040$. With Model B, the parameter for $I = 0$ was reduced to $S_{I=0} = 0.721 \pm 0.016$, whereas the parameter for $I = 1$ was increased to $S_{I=1} = 1.423 \pm 0.055$. Considering each figure, the $I = 1$ spectrum appears to be in good agreement with both Models A and B. On the other hand, the spectra for the interference term and $I = 0$ seem to align reasonably well with Model B, but not with Model A. In Model A, the fit for the interference term appears to lack intensity above the threshold, and the overall spectrum does not seem to match $I = 0$. In fact, the fitting with Model B yields $\chi^2/NDF = 220/42 = 5.25$, whereas the fitting with Model A is significantly worse, with $\chi^2/NDF = 691/42 = 16.4$. Table 5.1 lists the pole parameters of $\Lambda(1405)$ derived from the DCC model, where Pole1, the higher of the two poles, significantly affects the observed spectrum. In model A, the imaginary part, or width, of that parameter is large, resulting in a pronounced tail of the $I = 0$ spectrum below the $\bar{K}N$ threshold, thus preventing accurate reproduction of the observed spectrum.

Table 5.1: This table shows the pole position with $I = 0$ and $J^P = 1/2^-$ below the $\bar{K}N$ threshold by DCC models [46]

	pole1	pole2
Model.A	$1437 - 75i$	$1372 - 56i$
Model.B	$1428 - 31i$	$1397 - 98i$

In more detail, the fitting in model B reveals that both the $I = 0$ and $I = 1$ spectra seem to lack intensity compared to the theoretical spectrum above the $\bar{K}N$ threshold, while the interference term spectrum shows a better fit. This means that the $I = 0$ spectrum is determined below the $\bar{K}N$ threshold, while above the $\bar{K}N$ threshold, it is limited by the interference between $I = 0$ and $I = 1$. In general, the scattering amplitude is complex, and there is flexibility to adjust its phase, i.e., to introduce a parameter representing the phase difference between $I = 0$ and $I = 1$. If the phase

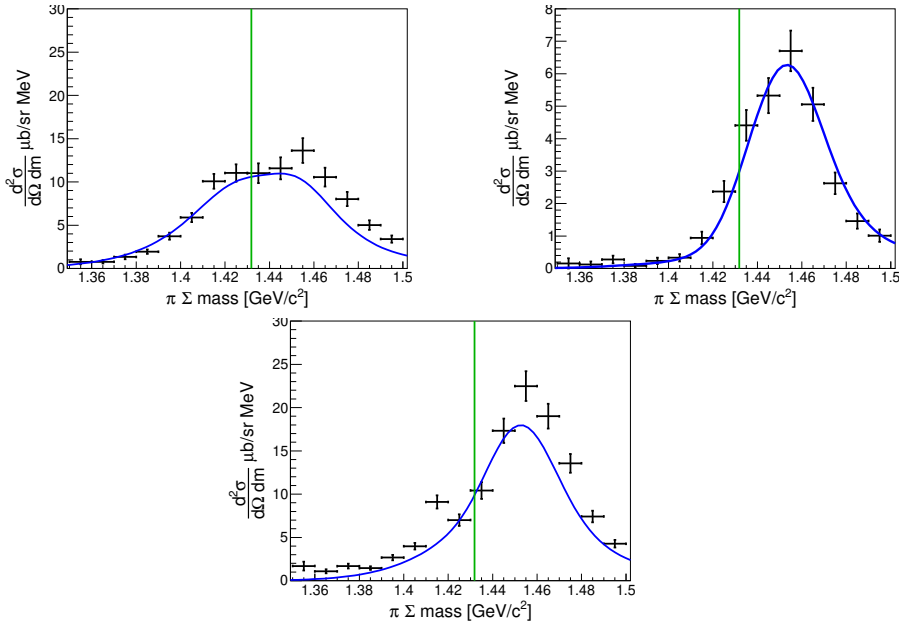


Figure 5.5: This figure shows the results of the fitting using Model.B with the introduction of parameters related to the interference term. The notation is the same as in Fig.5.4. In this fitting, the $I = 1$ strength is determined only from the $\pi^- \Sigma^0$ spectrum, while the other two parameters are determined from the $\pi^- \Sigma^+$ and $\pi^+ \Sigma^-$ spectra.

difference is denoted by $\theta_{I=0,1}$, the relationship between the scale parameter, which modifies the magnitude of the interference term, and $S_{int} = \cos \theta_{I=0,1}$ can be derived from the third term in Eq.5.1.

We fit the observed spectrum with DCC's Model B by introducing a free parameter that adjusts this interference term independently. The $I = 1$ spectrum is determined only from the $\pi^-\Sigma^0$ spectrum, whereas the $I = 0$ spectrum is derived from all three $\pi\Sigma$ spectra. The interference term is determined from the $\pi^-\Sigma^+$ and $\pi^-\Sigma^-$ spectra. Therefore, we first fit only the $I = 1$ spectrum, fixed $S_{I=1}$ at that value, and then performed a fit to determine both $S_{I=0}$ and S_{int} , as shown in Figure 5.5. The $\chi^2/NDF = 187/41 = 4.56$ of this fit is, which was improved by introducing a phase parameter. In this fit, the $I = 0$ scale parameter $A_{I=0}$ decreases from 0.721 ± 0.016 to 0.686 ± 0.017 , while the $I = 1$ parameter $A_{I=1}$ increases from 1.423 ± 0.055 to 1.462 ± 0.059 . The interference term A_{int} is estimated as 0.828 ± 0.030 and weakened. This value corresponds to a phase difference of $\delta\theta_{I=0,1} = 34.1^{+3.0}_{-3.2}[\text{degree}]$ between the $I = 0$ and $I = 1$ interference terms. This is considered to be due to the increase in $I = 1$, which is primarily structured above the $\bar{K}N$ threshold, being balanced by the intensity above the $\bar{K}N$ threshold for $I = 0$.

Finally, there is room to further improve the fit by simultaneously fitting all parameters. The result is shown in Figure 5.6, where $\chi^2/NDF = 184/41 = 4.48$, and no significant improvement is observed. This suggests that $A_{I=1}$ is determined from a single spectrum. Compared to the case where $A_{I=1}$ was determined first, the parameters in this case show that $A_{I=0}$ decreased from 0.686 ± 0.017 to 0.682 ± 0.017 , $A_{I=1}$ increased from 1.462 ± 0.059 to 1.570 ± 0.058 , and A_{int} decreased slightly from 0.828 ± 0.030 to 0.811 ± 0.030 , in the same direction as the introduction of A_{int} . This value of A_{int} corresponds to a phase $\theta = 0.811 \pm 0.030$ shift.

5.1.3 $\bar{K}N$ Pole parameters assuming the 2-step reaction

Next, we discuss the method for obtaining the $\bar{K}N$ pole parameters through fitting under the assumption of a 2-step reaction. This approach is similar to that used by Noumi et al., as introduced in Chapter 1. Since this analysis method focuses only on $I = 0$, the obtained spectra are separated into components of $I = 0$. In this procedure, the spectra are further separated into components of $I = 1$ and, in addition, the interference term between $I = 0$ and $I = 1$. The obtained spectrum can be expressed as follows from the isospin relation.

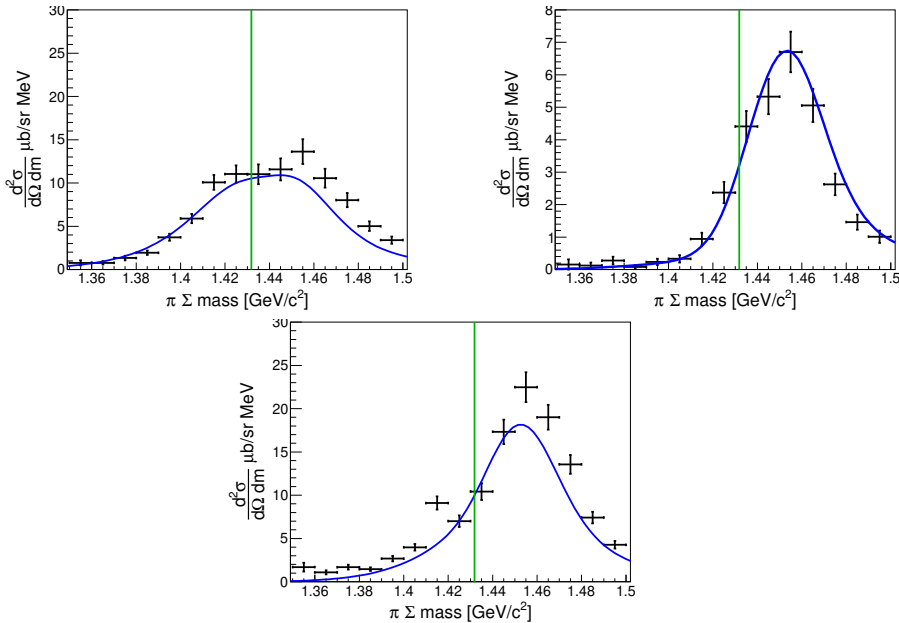


Figure 5.6: This figure shows the results of the fitting using Model.B with the introduction of parameters related to the interference term. The notation is the same as in Fig.5.4. All three parameters are determined simultaneously in this fitting.

$$\begin{aligned} \frac{d\sigma}{d\Omega dM}(\pi^\mp \Sigma^\pm) &\propto |C_{K^-N \rightarrow \bar{K}N}^0 T_{\bar{K}N \rightarrow \pi\Sigma}^{I=0} \mp C_{K^-N \rightarrow \bar{K}N}^1 T_{\bar{K}N \rightarrow \pi\Sigma}^{I=1}|^2 \\ &= |C_{K^-N \rightarrow \bar{K}N}^0 T_{\bar{K}N \rightarrow \pi\Sigma}^{I=0}|^2 + |C_{K^-N \rightarrow \bar{K}N}^1 T_{\bar{K}N \rightarrow \pi\Sigma}^{I=1}|^2 \\ &\mp 2\text{Re}(C_{K^-N \rightarrow \bar{K}N}^0 C_{K^-N \rightarrow \bar{K}N}^1 T_{\bar{K}N \rightarrow \pi\Sigma}^{I=0} T_{\bar{K}N \rightarrow \pi\Sigma}^{I=1}) \end{aligned} \quad (5.1)$$

$$\frac{d\sigma}{d\Omega dM}(\pi^- \Sigma^0) \propto |C_{K^-N \rightarrow \bar{K}N}^1 T_{\bar{K}N \rightarrow \pi\Sigma}^{I=1}|^2 \quad (5.2)$$

Here, $T_{\bar{K}N \rightarrow \pi\Sigma}^{I=0,1}$ represents the T matrix of the second $\bar{K}N \rightarrow \pi\Sigma$ scattering for isospin $I = 0$ and $I = 1$. Additionally, $C_{K^-N \rightarrow \bar{K}N}^{0,1}$ denotes the factor for the first $K^- p \rightarrow \bar{K}N$ scattering, corresponding to the isospin $I = 0$ and $I = 1$ components of the second scattering.

Since it can be expressed as shown in Equation (5.1), (5.2), the spectra corresponding to $I = 0$, $I = 1$, and their interference terms can be written as follows.

$$\frac{d\sigma}{d\Omega dM}(I = 0) \propto \frac{1}{2} \left(\frac{d\sigma}{d\Omega dM}(\pi^- \Sigma^+) + \frac{d\sigma}{d\Omega dM}(\pi^+ \Sigma^-) - \frac{d\sigma}{d\Omega dM}(\pi^- \Sigma^0) \right) \quad (5.3)$$

$$\frac{d\sigma}{d\Omega dM}(I = 1) \propto \frac{d\sigma}{d\Omega dM}(\pi^- \Sigma^0) \quad (5.4)$$

$$\frac{d\sigma}{d\Omega dM}(\text{int}) \propto \left(\frac{d\sigma}{d\Omega dM}(\pi^- \Sigma^+) - \frac{d\sigma}{d\Omega dM}(\pi^+ \Sigma^+) \right) \quad (5.5)$$

The 2-step response can be expressed as follows,

$$\frac{d\sigma}{dM_{\pi\Sigma} d\Omega_n} = \left| \langle n_{\theta=0} \pi\Sigma | T_{\bar{K}N_2 \rightarrow \pi\Sigma}^2 G_0(\bar{K}, N_2) T_{K^-N_1 \rightarrow \bar{K}N}^1 | K^- \Phi_d \rangle \right|^2$$

where $G_0(\bar{K}, N_2)$, represents the Green's function describing the propagation of virtual \bar{K} mesons between the first and second scattering steps. This equation can be factorized using the deuterium wavefunction $\psi_d(p)$ and decomposed into a 1-step response $f_{res}(M_{\pi\Sigma})$ function and a 2-step scattering amplitude as shown below.

$$\begin{aligned} \frac{d\sigma}{dM_{\pi\Sigma} d\Omega_n} &\sim \left| T_{\bar{K}N_2 \rightarrow \pi\Sigma}^2 \right|^2 F_{res}(M_{\pi\Sigma}) \\ F_{res}(M_{\pi\Sigma}) &= \left| \int G_0(\bar{K}, N_2) T_{K^-N \rightarrow \bar{K}N}^1 \psi_d(p) d^3 p_N \right|^2 \end{aligned}$$

The T -matrix of the second scattering is expressed as follows, utilizing the

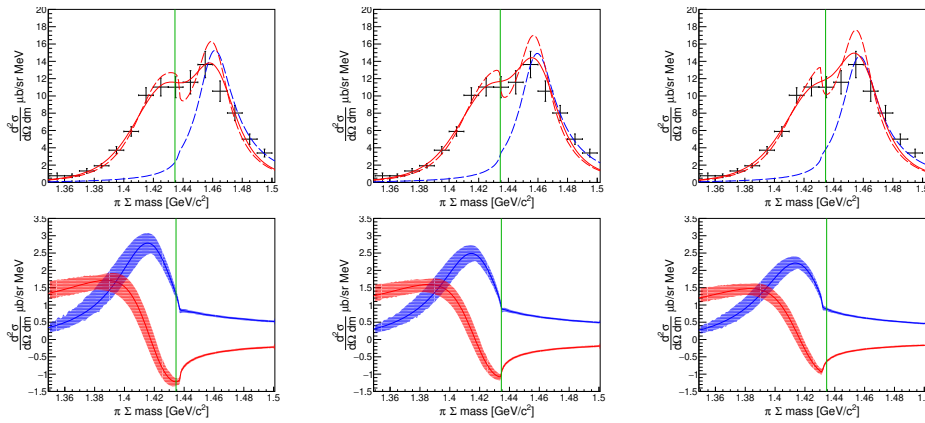


Figure 5.7: This figure shows the $I = 0$ spectrum obtained from Eq. (5.3) and the fit results assuming a 2-step reaction. In the upper panel, the error bars represent the experimental data, the red line indicates the spectrum resulting from the fit, the solid line corresponds to the spectrum convolved with detector resolution, and the dashed line represents the spectrum without resolution. The lower panel displays the scattering amplitude for the two-step $\bar{K}N \rightarrow \bar{K}N$ scattering, where the red line indicates the real part and the blue line shows the imaginary part. The lines are the best-fit values and the bands hatched in color represent the width of the error due to fitting.

low-energy expansion up to the second order for the two channels [67].

$$T_{\bar{K}N \rightarrow \bar{K}N}^2 = \frac{A}{1 - iAk_2 + \frac{1}{2}ARKk_2^2}$$

$$T_{\bar{K}N \rightarrow \pi\Sigma}^2 = \frac{e^{i\delta}}{\sqrt{k_1}} \frac{\sqrt{\text{Im}A - \frac{1}{2}|A|^2\text{Im}Rk_2^2}}{1 - iAk_2 + \frac{1}{2}ARKk_2^2}$$

This fit includes the scattering length A and the effective range R of the second-step scattering, along with a parameter determining the overall scale. In other words, the shape of the first-step scattering (reaction function) is fixed, and the spectrum shape is determined solely by the second-step scattering. The scattering length and effective range are complex numbers, so there are five free parameters in total. This fitting is performed using three $\bar{K}N$ threshold values: K^-p , $\bar{K}N$ (the average of K^-p and K^0n), and K^0n . The discrepancies in the results arising from the differences in threshold values are evaluated as a source of systematic error. These differences in threshold values are reflected not only in the mass of the $\bar{K}N$ channel in the T -matrix of the seccond-scattering but also in the mass of the nucleon used to calculate the response function in the first-step scattering. The figure above shows the results of the fit: black error bars represent the data, and the red solid line shows the fit results convolved with detector resolution, which are used to calculate the chi-square. The red dashed line shows the fit spectrum without detector resolution, and the blue dashed line indicates the response function, scaled arbitrarily. The figure below shows the scattering amplitude obtained from the fit, with red and blue representing the real and imaginary parts, respectively. The lines indicate the best-fit result, and the bands show the error range, determined by the maximum and minimum values when adjusting the real and imaginary parts of A and R within their error margins. The central values of the parameters and the fitting errors were evaluated in terms of the average $\bar{K}N$ threshold, with $A = -1.05 \pm 0.12(\text{fit.}) \pm +0.09(\text{syst.}) + [0.86 \pm 0.15(\text{fit.})]^{+0.07}_{-0.08}(\text{syst.})i$ and $R = -0.22 \pm 0.40(\text{fit.})]^{+0.05}_{-0.06}(\text{syst.}) + [-0.42 \pm 0.16(\text{fit.})]^{+0.12}_{-0.08}(\text{syst.})i$. These values need to be converted to the pole 's position [MeV] and width [MeV], where the pole is defined by setting the denominator of the T -matrix to zero, i.e., by solving the following equation.

$$\frac{1}{2}ARKk^2 + Ak^2 + 1 = 0 \quad (5.6)$$

Where k is the momentum of the $\bar{K}N$ center-of-mass system, converted to mass by $m = \sqrt{m_{\bar{K}N}^2 + k^2}$.

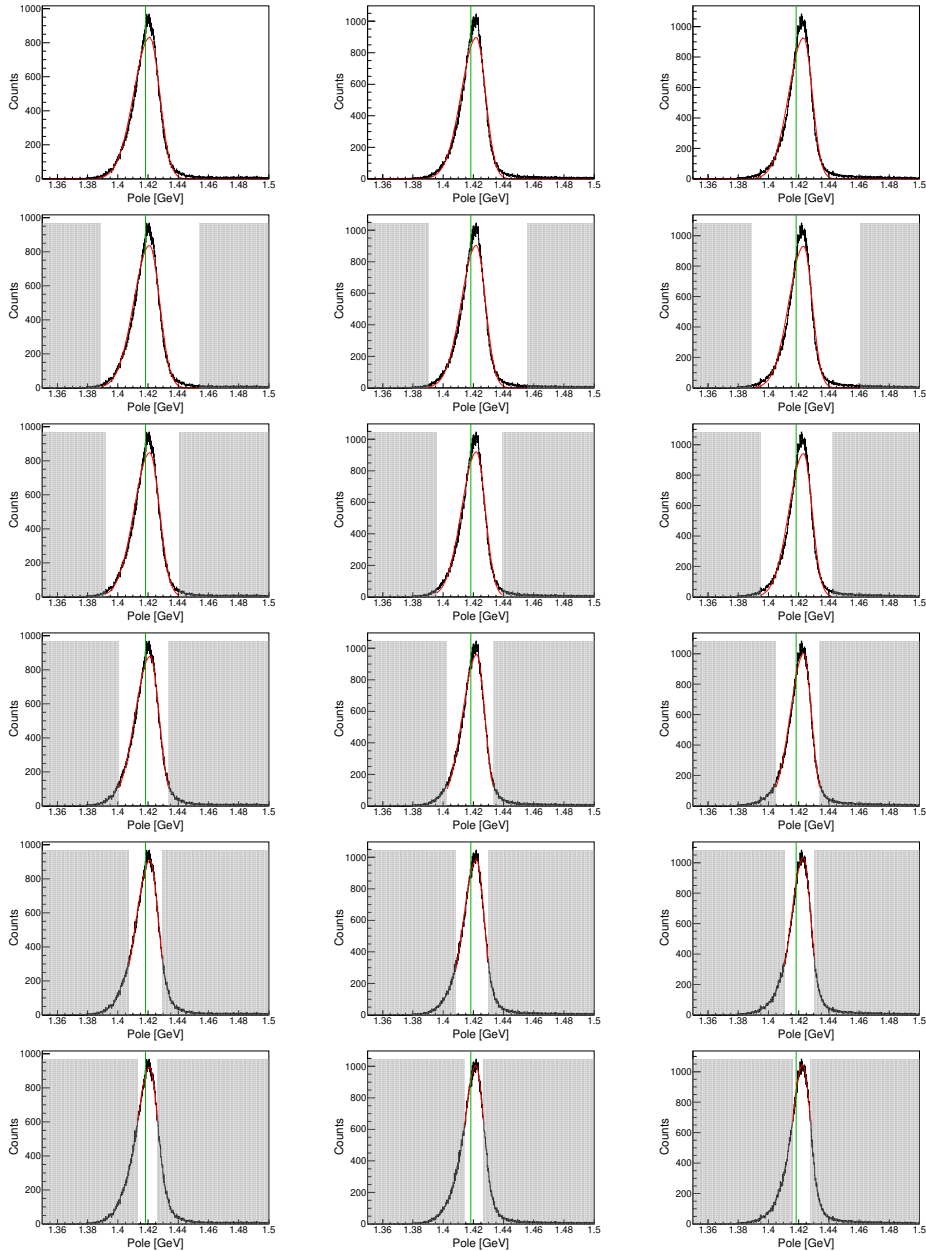


Figure 5.8: This figure shows the distribution and fit of the poles of $\Lambda(1405)$, generated using Gaussian random numbers. The right, center, and left panels correspond to the results based on the $K^- p$, $\bar{K}N$, and $K^0 n$ thresholds, respectively. The top row represents the fit over the entire range, followed by rows corresponding to the equivalent ranges of 3σ , 2.5σ , 2σ , 1.5σ , and 1σ . The fit results are shown as red lines, with gray hatched areas representing regions excluded from the fit. The green lines indicate the pole positions corresponding to the best-fit values shown in Figure 5.7.

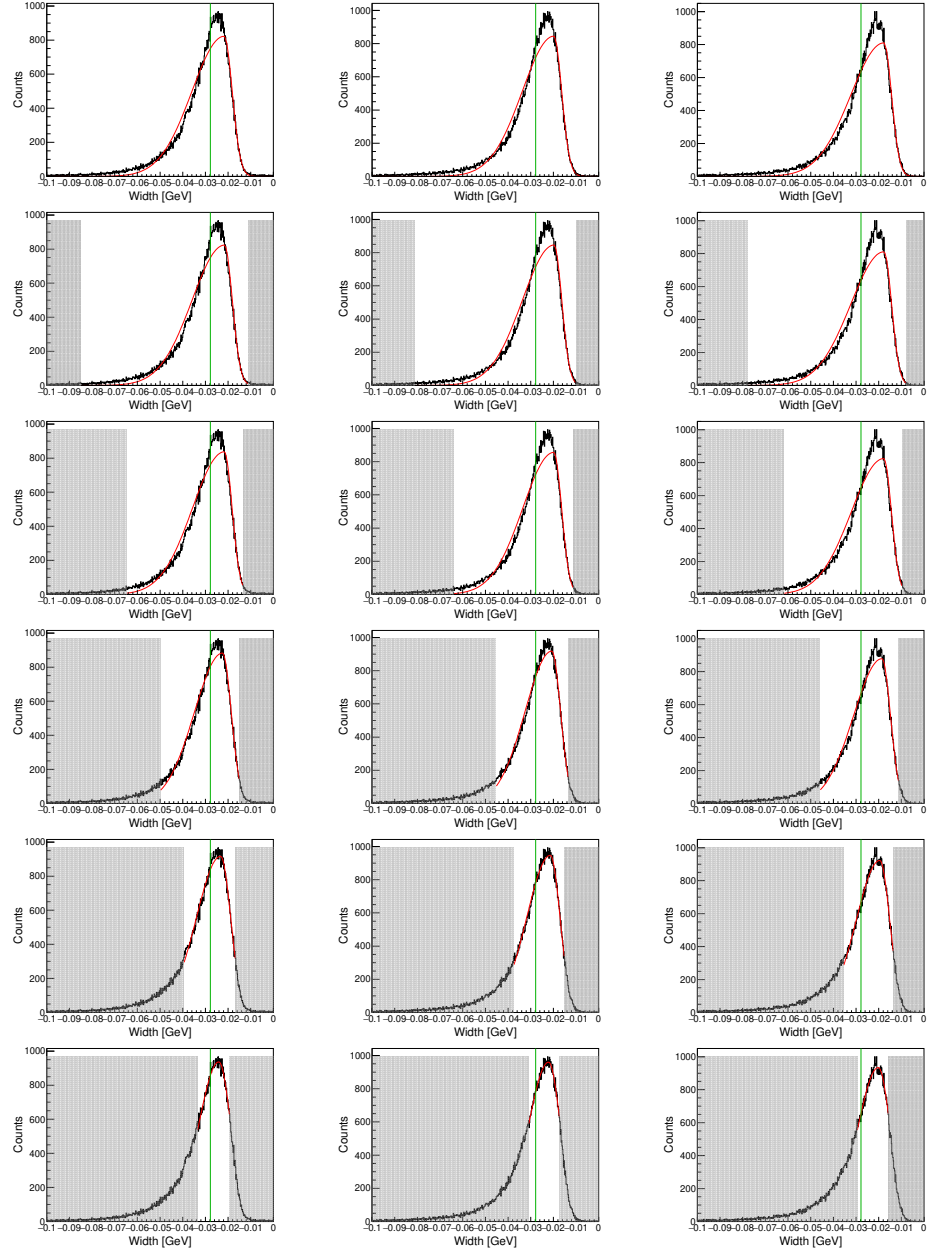


Figure 5.9: This figure shows the distribution and fit of the widths of $\Lambda(1405)$, generated using Gaussian random numbers. The details of the figure caption are identical to those of Figure 5.8, which provides further context.

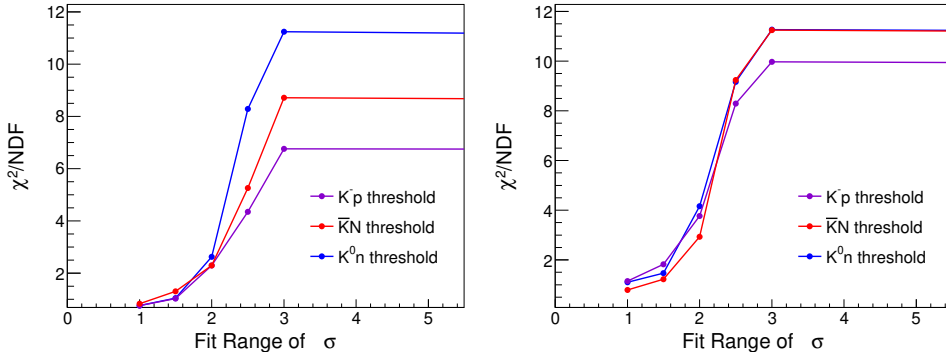


Figure 5.10: This figure illustrates the χ^2/NDF relationship for the fittings of the $\Lambda(1405)$ pole and width, as shown in Figures 5.8 and 5.9. The left panel corresponds to the pole fittings, while the right panel represents the width fittings. The purple, red, and blue lines indicate the results for the $K^- p$, $\bar{K} N$, and $K^0 n$ thresholds, respectively.

Since A and R are complex numbers, propagating their errors is not straightforward. Therefore, the position and width errors of the poles are estimated by generating a Gaussian distribution using the real and imaginary parts of A and R as random variables, with fitting errors as the standard deviation σ . This approach is similar to the conventional error propagation method, which treats each parameter as an independent Gaussian, with the overall error as a composite of Gaussian distributions. Figure 5.8, 5.9 shows the resulting distribution of position and width. These distributions are clearly asymmetric, particularly in terms of width, due to a threshold effect caused by the proximity of the thresholds.

$$f_{fit}(x) = \begin{cases} A \exp\left(-\frac{(x-M)^2}{2\sigma_h^2}\right) & (x > M) \\ A \exp\left(-\frac{(x-M)^2}{2\sigma_l^2}\right) & (x < M) \end{cases}$$

Here, M represents the central value, with σ_h and σ_l denoting the errors in the high and low regions, respectively. This function explicitly distinguishes between errors above and below the central value while ensuring continuity at M . The distribution includes a tail component that deviates from a Gaussian profile, which must be excluded for accurate error evaluation. To achieve this, the evaluation range is divided into several regions, each corresponding to a percentage of the peak height, and the fit is performed in each region. For instance, $\exp(-\frac{1}{2}3^2)$ corresponds to the $\pm 3\sigma$ region. This fitting process was conducted for all regions, ranging from 3σ to 1σ , with

increments of 0.5σ . Figure 5.10 shows the relationship between the reduced χ^2/NDF and the cut range for each fit. Here, the χ^2/NDF increases from the entire region to 3σ . This is thought to be due to the limited improvement in the fit because the tail component was not fully removed, as well as the decrease in NDF resulting from the narrower range. The χ^2/NDF seems to reach saturation at the 1.5σ range. Therefore, a range of 1.5σ is chosen as a reference to determine the position and width of the pole of $\Lambda(1405)$, which is found to be $1418.3^{+7.5}_{-2.4}(fit.)^{+0.9}_{-1.1}(syst.) + [-27.8^{+9.5}_{-0.9}(fit.)^{+1.9}_{-2.1}(syst.)]i$ [MeV]. Here, the central value is determined from the scattering length and the effective range of the best fit. The fitting errors are evaluated using the average of K^0n and K^-p for the threshold values, and the systematic errors were assessed by varying the threshold values.

Chapter 6

Conclusion

Appendix A

$\pi^0 \Sigma^0$ spectrum analysis

Appendix B

Detector resolution

The resolution of the final $\pi\Sigma$ spectrum can be categorized into two main sources: one originating from the CDS and the other from the forward detector system. The resolution of each detector was estimated by reproducing the mass distribution of known particles measured in our experiments, and these values were used to estimate the resolution of the final pi-Sigma spectrum.

B.1 CDC resolution

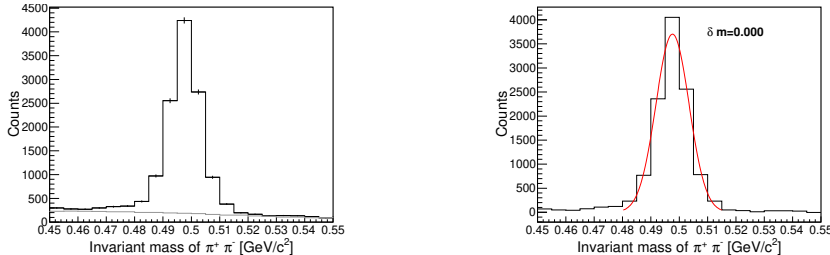


Figure B.1: These figures show the $K^0 \rightarrow \pi^+\pi^-$ decay peak in $K^-d \rightarrow n\pi^+\pi^n$ events. The left figure displays the $K^-d \rightarrow n\pi^+\pi^-n$ event spectrum (black line) along with the MC simulated background (gray line). The right figure presents the background-subtracted spectra and the fit results.

As explained in Section ??, the CDS measures the momentum of charged particles by tracking their trajectories in a magnetic field. The resolution of the CDS is estimated using events in which the K^0 produced in the $K^-d \rightarrow nnK^0$ reaction decays into π^+ and π^- . This reaction is one of the

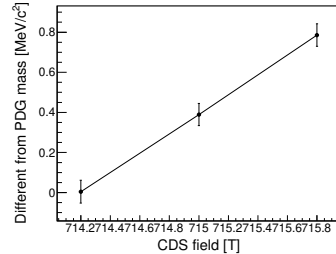


Figure B.2: This figure shows the relationship between the magnetic field settings of the CDS in the analysis and the center value of the K^0 peak.

$K^- d \rightarrow n\pi^+\pi^-n$ final states described in Section 4.1, and this final state is fully reconstructed as explained in Section 4.1.2. Therefore, by subtracting reactions other than K^0 production, only the peak can be extracted, as shown in Figure. B.1. The magnetic field of the CDS is measured using a Hall probe, and fine-tuning is performed based on the K^0 peak. As shown in the Figure B.2, this was done using selected values of the CDS magnetic field applied in the experimental data analysis. The field was slightly adjusted from the default value of ???T and was finally determined to be ???T.

The momentum resolution is based on the positional resolution of the CDC. To determine the positional resolution that best reproduces the width of the observed K^0 peak, the correlation between the positional resolution of the CDC and the width of the K^0 peak in the MC simulation was examined, as shown in Figure ???. From this, the positional resolution was estimated to be $200\mu m$.

B.2 Detector resolution on the $d(K^-, N)$

Appendix C

$d(K^-, n)K^0 n$ analysis

Bibliography

- [1] R.L. Workman et al. (Particle Data Group), Prog. Theor. Exp. Phys. 2022, 083C01 (2022)
"Review of Particle Physics"
- [2] R. H. Dalitz and A. Deloff, J. Phys. G17, 281 (1991).
"The Shape and Parameters of the $\Lambda(1405)$ Resonance"
- [3] M. Hassanvand et el., Phys. Rev. C **87**, 055202 (2013)
"Theoretical analysis of $\Lambda(1405) \rightarrow (\pi\Sigma)^0$ mass spectra produced in $p + p \rightarrow p + \Lambda(1405) + p$ reactions"
- [4] J. Esmaili, Y. Akaishi, and T. Yamazaki, Phys. Lett. B **686**, 23 (2010)
"Experimental confirmation of the $\Lambda(1405)$ ansatz from resonant formation of a K^-p quasi-bound state in K^- absorption by ${}^3\text{He}$ and ${}^4\text{He}$ "
- [5] R. H. Dalitz and S. F. Tuan, Phys. Rev. Lett. 2 (1959).
"Possible Resonant State in Pion-Hyperon Scattering"
- [6] M. H. Alston, L. W. Alvarez, P. Eberhard and M. L. Good, Phys. Rev. Lett. 6, 698 (1961).
"Study of Resonances of the Σ - π System"
- [7] R. J. Hemingway, Nucl Phys B **253**, 742 (1985).
"Production of $\Lambda(1405)$ in K^-p Reactions at $4.2\text{GeV}/c$ "
- [8] B. Conforto et el., Nucl. Phys. B **34**, 41 (1971).
"New experimental results on the Reactions $K^-p \rightarrow \bar{K}N$ and $K^-p \rightarrow \Sigma\pi$ a partial-wave analysis between 430 and $800\text{MeV}/c$ "
- [9] A. J. Van Horn, Nucl. Phys. B **87**, 145 (1975).
"Energy dependent partial-wave analysis of $K^-p \rightarrow \Lambda\pi^0$ between 1540 and 2215MeV "

- [10] R. J. Hemingway et el., Nucl. Phys. B **91**, 12 (1975).
"New data on $K^- p \rightarrow K^- p$ and $K^0 n$ and a partial-wave analysis between 1840 and 2234 MeV center of mass energy"
- [11] P. Baillon and P. J. Litchfield, Nucl. Phys. B **94**, 39 (1975).
"Energy-independent partial-wave analysis of $\bar{K}N \rightarrow \Lambda\pi$ between 1540 and 2150 MeV"
- [12] G. P. Gopal et al., Nucl. Phys. B **119**, 362 (1977).
"Partial-wave analyses of KN two-body reactions between 1480 and 2170 MeV"
- [13] M. Sakitt et al., Phys. Rev. **139**, B179
"Low-Energy K^- Meson Interactions in Hydrogen"
- [14] J. K. Kim, Phys. Rev. Lett. **19**, 1074 (1967).
"Multichannel Phase-Shift Analysis of $\bar{K}N$ Interaction in the Region 0 to 550 MeV/c"
- [15] A. D. Martin, Nucl. Phys. B **179**, 33 (1981).
"Kaon-Nucleon Parameters"
- [16] P. B. Siegel and W. Weise, Phys. Rev. C **38**, 2221 (1988).
"Low-energy K^- -nucleon potentials and the nature of the $\Lambda(1405)$ "
- [17] J. D. Davies et al., Phys. Lett. B **83**, 55 (1979).
"Observation of kaonic hydrogen atom X-rays"
- [18] M. Izycki et al., Z. Phys. A **297**, 11 (1980).
"Results of the search for K -series X-rays from kaonic hydrogen"
- [19] P. M. Bird et al., Nucl. Phys. A **404**, 482 (1983).
"Kaonic Hydrogen atom X-rays"
- [20] M. Iwasaki et al., Phys. Rev. Lett. **78**, 3067 (1997).
"Observation of Kaonic Hydrogen K_α X Rays"
- [21] M. Bazzi et al., Phys. Lett. B **704**, 113 (2011).
"A New Measurement of Kaonic Hydrogen X-Rays"
- [22] J.C.Nacher et al., Phys. Lett. B **455**, 55 (1999).
"Photoproduction of the $\Lambda(1405)$ on the proton and nuclei"

- [23] M. Niiyama et al., Phys. Rev. C **78**, 035202 (2008).
"Photoproduction of $\Lambda(1405)$ and $\Sigma(1385)$ on the proton at $E_\gamma = 1.5\text{-}2.4\text{GeV}/c$ "
- [24] K. Moria for the CLAS Collaboration,
Phys. Rev. C **87**, 035206 (2013).
"Measurement of the $\pi\Sigma$ photoproduction line shapes near the $\Lambda(1405)$ "
- [25] K. Moria for the CLAS Collaboration,
Phys. Rev. Lett. **112**, 082004 (2014).
"Spin and parity measurement of the $\Lambda(1405)$ baryon"
- [26] S. X. Nakamura, and D. Jido, Prog. Theor. Exp. Phys., 023D01 (2014)
"Lambda (1405) photoproduction based on the chiral unitary model"
- [27] D. Jido et al., Nucl. Phys. A **725**, 181 (2003).
"Chiral Dynamics of the Two $\Lambda(1405)$ States"
- [28] G. Agakishiev for the HADES Collaboration,
Phys. Rev C **87**, 025201 (2013).
"Baryonic Resonances to the $\bar{K}N$ threshold: The case of $\Lambda(1405)$ in pp collisions"
- [29] Y. Ikeda, T. Hyodo, and W. Weise, Nucl. Phys. A **881**, 98 (2012)
"Chiral SU(3) theory of antikaon–nucleon interactions with improved threshold constraints"
- [30] Z.-H. Guo and J. Oller, Phys. Rev. C **87**, 3, 035202 (2013)
"Meson-baryon reactions with strangeness - 1 within a chiral framework"
- [31] M. Mai and U.-G. Meißner, Eur. Phys. J. A **51**, 3, 30 (2015),
"Constraints on the chiral unitary amplitude from $\pi\Sigma K^+$ photoproduction data"
- [32] H. Zhang et al., Phys. Rev. C **88**, 035204 (2013).
"Partial-wave analysis of $\bar{K}N$ scattering reactions"
- [33] H. Zhang et al., Phys. Rev. C **88**, 035205 (2013).
"Multichannel parametrization of $\bar{K}N$ scattering amplitudes and extraction of resonance parameters"
- [34] H. Kamano et al., Phys. Rev. C **90**, 065202 (2014).
"Dynamical Coupled-Channels Model of K^-p Reactions:

- Determination of partial wave amplitudes”
 Phys. Rev. C**92**, 025205 (2015).
- ”Dynamical Coupled-Channels Model of $K^- p$ Reactions.
 Extraction of Λ^* and Σ^* Hyperon Resonances”
 Phys. Rev. C**95**, 044903(E) (2015).
- [35] G. Beer et al., Phys. Rev. Lett. **94**, 212302 (2005).
 ”Measurement of the Kaonic Hydrogen X-Ray Spectrum”
- [36] S. Deser et al., Phys. Rev. **96**, 774 (1954).
 ”Energy Level Displacements in Pi-Mesonic Atoms”
- [37] T.L. Trueman, Nucl. Phys. **26**, 57 (1961).
 ”Energy level shifts in atomic states of strongly-interacting particles”
- [38] O. Braun et al., Nucl. Phys. B **129**, 1 (1977).
 ”New Information About the Kaon-Nucleon-Hyperon Coupling Constants $g(KN\Sigma(1197))$, $g(KN\Sigma(1385))$ and $g(KN\Lambda(1405))$ ”
- [39] D. Jido, E. Oset and T. Sekihara, Eur. Phys. J. A **42**, 257 (2009).
 ”Kaonic Production of $\Lambda(1405)$ off deuteron target in chiral dynamics”
- [40] J. Yamagata-Sekihara, T. Seki hara, and D. Jido, Prog. Theor. Exp. Phys. **2013**, 043D02 (2013).
 ”Production of hyperon resonances induced by kaons on a deuteron target”
- [41] H. Noumi et al., Proposals for the 15th PAC meeting
 ”Spectroscopic study of hyperon resonances below $\bar{K}N$ threshold via the (K^-, n) reaction on Deuteron”
- [42] K. Miyagawa, J. Haidenbauer, and H. Kamada Phys. Rev. C **97**, 055209 (2018)
 ”Faddev approach to the reaction $K - d \rightarrow \pi\Sigma n$ at $p_K = 1.0 GeV/c$ ”
- [43] E. Oset, A. Ramos, and C. Bennhold, Phys. Lett. B **527**, 99 (2002);
530, 260(E) (2002).
 ”Low lying $S = -1$ excited baryons and chiral symmetry”
- [44] A. Cieplý and J. Smejkal, Nucl. Phys. A **881**, 115 (2012).
 ”Chirally motivated $\bar{K}N$ amplitudes for in-medium applications”

- [45] S. Ohnishi et el, Phys. Rev. C **93**, 025207 (2016).
"Strcture of the $\Lambda(1405)$ and the $K^-d \rightarrow \pi\Sigma n$ reaction"
- [46] H. Kamano et el., Phys. ReV. **C94**, 065205 (2016).
"Toward Establishing Low-Lying Λ and Σ Hyperon Resonances with the $\bar{K} + d \rightarrow \pi + Y + N$ Reaction"
- [47] H. Noumi for the E31 Collaboration, Phys. ReV. **B837**, 137637 (2023).
"Pole Position of $\Lambda(1405)$ measured in $d(K^-, n)\pi\Sigma$ reaction"
- [48] S. Kawasaki's Doctor thesis will be submitted.
- [49] K. Agari et el, Prog. Theor. Exp. Phys., 02B009 (2012)
- [50] K. Agari et el, Prog. Theor. Exp. Phys., 02B011 (2012)
- [51] TRANSPORT <http://linac96.web.cern.ch/Linac96/Proceedings/Thursday/THP72/Paper.pdf>
- [52] T. K. Ohska et al., Nuclear Science, IEEE Transactions on **33**, 98 (1986).
- [53] M. Shiozawa and et el., A new TKO system manager board for a dead-time-free data acquisition system, in 1994 IEEE Nuclear Science Symposium-NSS'94, pages 632–635, (1994)
- [54] M. Iio et al., Nucl. Instrum. Methods Phys. Res., Sect. **A** **687**, 1 (2012).
- [55] S. Agostinelli et al., Nucl. Instrum. Methods Phys. Res., Sect. **A** **506**, 250 (2003)
J. Allison et el., IEEE Transactions on Phys. Sci. **53**, 207 (2006)
J. Allison et al., Nucl. Instrum. Methods Phys. Res., Sect. **A** **835**, 186 (2016)
- [56] K. Fuji, https://www-jlc.kek.jp/subg/offl/lib/docs/helix_manip/node3.html (1968).
- [57] Opera Electromagnetic FEA Solution Software
- [58] V. Flaminio et al., CERN-HARA-87-01, 121 (1983).
- [59] M. Jones et el, Nucl. Phys. B **90**, 349 (1975)
- [60] R. Barlow and C. Beeston, Comp. Phys. Comm. **77**, 219 (1993).
"Fitting using finite Monte Carlo samples"
- [61] A. Nappi, Comp. Phys. Comm. **180**, 269 (2009).

- [62] C.J.S. Damerell et. el., Nucl. Phys. **B129**, 397 (1977). " K^-n elastic scattering between 610 and 840 MeV/c"
- [63] M. Jones, R. Levi, Setti, D. Merrill and R. D. Tripp, Phys. Rev. **B90**, 349 (1975). K^-p charge exchange and hyperon production cross section from 860 to 1000 MeV/c
- [64] M. Bernheim and et. el., Nucl. Phys. **A365**, 349, (1981). Momentum distributions of nucleons in the deuteron from $d(e, e'p)n$ reaction
- [65] R. Machleidt, Phys. Rev. **C63**, 024001 (2001).
- [66] R. Barlow and C. Beeston, Comp. Phys. Comm. **77**, 219 (1993).
- [67] L. Lensniak, AIP Conf. Proc. 1030, 238–243 (2008). New formula for a resonant scattering near an inelastic threshold
- [68] S. Agostinelli et al., Nuclear Instruments and Methods in Physics Research Section A: Accelerators, Spectrometers, Detectors and Associated Equipment **506**, 250 (2003).
J. Allison et al., Nuclear Instruments and Methods in Physics Research Section A: Accelerators, Spectrometers, Detectors and Associated Equipment **835**, 186 (2016).